Modeling and Indirect Force/Position Control of Slender Continuum Robots

Amir Molaei

A Thesis

in

The Department

of

Mechanical, Industrial and Aerospace Engineering

Presented in Partial Fulfillment of the Requirements

for the Degree of

Doctor of Philosophy (Mechanical Engineering) at

Concordia University

Montréal, Québec, Canada

June 2022

CONCORDIA UNIVERSITY

School of Graduate Studies

This is to certify that the thesis prepared

By: **Mr. Amir Molaei**

Entitled: **Modeling and Indirect Force/Position Control of Slender Continuum Robots**

and submitted in partial fulfillment of the requirements for the degree of

Doctor of Philosophy (Mechanical Engineering)

complies with the regulations of this University and meets the accepted standards with respect to originality and quality.

Signed by the Final Examining Committee:

_____ Chair
Dr. Bruno Lee

_____ External Examiner
Dr. Mahdi Tavakoli

_____ External Examiner
Dr. Abdessamad Ben Hamza

_____ Examiner
Dr. Mojtaba Kheiri

_____ Examiner
Dr. Brandon Gordon

_____ Co-Supervisor
Dr. Javad Dargahi

_____ Co-supervisor
Dr. Amir G. Aghdam

Approved by: _____
Martin D. Pugh, Chair
Department of Mechanical, Industrial and Aerospace Engineering

2022 _____
Mourad Debbabi, Dean
Faculty of Engineering and Computer Science

Abstract

Modeling and Indirect Force/Position Control of Slender Continuum Robots

Amir Molaei, Ph.D.

Concordia University, 2022

In this thesis, a novel semi-analytical method is proposed for the pseudo-rigid body (PRB) modeling of highly flexible slender continuum robots (CRs) with no constraint on the number of degrees of freedom of the PRB model. The proposed method has a simple formulation and high precision. Furthermore, it can describe initially-curved variable-length CRs having a variable stiffness along the length. The versatility of the method is investigated for the PRB modeling of the slender CRs, such as steerable catheters and concentric tubes. A new analytical formulation is also introduced for the Cartesian stiffness of the CRs using the proposed PRB model. The existing formulations for the Cartesian stiffness in the literature, such as enhanced stiffness and constant stiffness models, fail to properly describe CRs force/deflection behavior with large nonlinear deformation. However, it is shown that the proposed method gives a high precision estimation of the applied force at the CR tip. Additionally, the proposed Cartesian stiffness is a function of deflection and allows indirect force estimation using the knowledge of only the tip point deflection, which makes it ideal for concentric tube robots (CTR) in vitreoretinal surgeries. The formulation of the stiffness is then used for the simultaneous force/position control of the CTRs interacting with a soft environment. The governing equation is a boundary value problem, and the existing control architectures for the simultaneous force/position control in rigid robotics cannot be directly used. Furthermore, in CTRs, the distributed friction force among the tubes and also at the entry port in vitreoretinal surgeries is beyond the desired force at the robot tip. Thus, the conventional method to map the task space forces to that of the joint space, which is fundamental in the existing force control methods, cannot be used. Therefore, a new control architecture is devised for the indirect hybrid force/position control of a variable-length initially-curved CTR. The proposed method uses displacement as the control input to the robot and proves effective for environments with a wide range of stiffness.

Acknowledgments

All through my life, I have had the privilege to benefit great mentors to whom I am indebted. Foremost, I would like to express my sincere gratitude to Mr. Hossein Samadi, the artist who shaped my character and gave me the chance and support to freely explore my curiosity while ignoring my mistakes. My growth and evolution as a designer, engineer, and researcher would have never been made possible without you. With faith, you have shaped my thinking and given me the courage to take risks driven by curiosity and curiosity alone.

I owe much gratitude to Professor Hamid Taghirad, my M.Sc supervisor, who brought me to the world of robotics. The robotics class I had with you was the most enjoyable class I have ever had, and my time in Advanced Robotic and Automation Systems (ARAS) labs, under your supervision, was the most memorable period of my studies. I am very proud to be a member of the large family of ARAS. It was in ARAS where I made my first working robot and found great friends. Thank you, Dr. Taghirad, for being such a great mentor and providing such a constructive lovely learning environment; you are a role model for my future academic career. I also wanted to thank my M.Sc advisor, Professor Mohammad A. Khosravi, for his ongoing support and friendship, from the early days I started my M.Sc studies. I am very grateful to have you as my friend and mentor.

I would like to thank Professor Javad Dargahi for his faith in me and for letting me discover solutions for open problems in robotics by giving me the chance to take risks in defining my research. Special thanks go to my second supervisor, Dr. Amir Aghdam, for his fatherly support and constructive criticism, who helped me to polish my ideas and be concise in research. I really appreciate your patience and being by my side through my research. I would like to express my

gratitude to the members of the examination committee, Dr. Mojtaba Kheiri, Dr. Brandon Gordon, Dr. Abdessamad Ben Hamza, and Dr. Bruno Lee, for their time and reviewing my thesis and their helpful guidance. Special thanks goes to Dr. Mahdi Tavakoli, my external committee member from University of Alberta. I would also like to thank the staff of the Mechanical, Industrial, and Aerospace Engineering Department for helping me to facilitate my studies.

I am deeply indebted to my colleagues and friends at the surgical robotic lab, Majid Roshanfar, Masoud Razban, and Mostafa Marzban. Special thanks go to Mostafa Marzban for his friendly support and his faith. I owe you a lot, and the success of my journey in extracurricular activities at Concordia was because of having a supportive friend like you. I would like to extend warm gratitude to my good friends and colleagues Nima and Kian, my undergraduate friends who were accompanying me at Surgical Robot Lab at Concordia. I am grateful to all of those with whom I have had the pleasure to work during my mandate at the Graduate Student Association. Special thanks go to Roozbeh Ghouchani, Duraichelvan Raju, and Aeisha Vyas for their constant support and friendship.

I would like to acknowledge the industrial companies I had the chance to work with during my studies, Cm-labs simulation, Symgery, and Touche Technologies. I very much appreciate Dr. Danial Alizadeh for supporting me to get my first job in Canada. Thank you for your faith in me and for giving me this opportunity. I would also like to thank my nice managers at Cm-Labs, Jean-Francois Emond and Mohammad Mohajerani. Thank you, Mohammad, for being such a flexible manager. I am very happy to work with you. Special thanks go to my countless colleagues in the Simulation Solution team, Farnood Gholami, Luc Phung, Bohan Sun, Robyn Yu, Mehdi Roozegar, Nila Nobari, Laszlo Kovacs, and Masoud Hassani. Cm-Labs was like a second university for me, and I would like to thank you all for being patient in answering my questions and helping me to grow. Thanks, Laszlo, for your time to review my Ph.D. research; your points helped me to be more concise. Masoud, my experience at Cm-labs simulation has become more enjoyable with your presence. The discussion I had with you on my thesis has helped me a lot with the difficulties I encountered in my thesis. Special thanks go to Thomas Friedlaender, director of innovation at Symgery, for his constant support and faith. I would also like to thank Kamran Ghaffari, the CEO of Touche Technologies; you're one of the greatest engineers I have had the privilege to collaborate

with. I am very happy to have had such a unique experience working closely with you.

I am grateful for the funding sources that allowed me to pursue my Ph.D. studies. I appreciate the Natural Sciences and Engineering Research Council of Canada (NSERC) for providing me the chance to be involved in the Surgical Innovation program. It was this program that helped me to deepen my clinical knowledge and made me familiar with the health system of Canada. Through this program, I had the chance to work in interdisciplinary teams and get involved with Canadian industries. I gratefully acknowledge FQRNT for their generous support throughout my Ph.D. studies. The moment I got to know that I am a recipient of this scholarship was one of the happiest moments I had in Canada. I also like to thank the public scholar program at Concordia University, which recognized the value of my work by giving me an opportunity to demonstrate it publicly. Thanks to Concordia University for awarding me a Student Tuition Award of Excellence, Doctoral Fellowship, Carolyn and Brian Neysmith Graduate Scholarships, and multiple Conference and Exposition Awards.

To my precious friend, Mohammad, thank you for your gift of friendship and for being there for me throughout my triumphs and my struggles. A warm expression of gratitude and love to my close friend from the first grade, Abbas. You are one of the most influential friends in my life; thanks for your constant presence. To Ebrahim, thanks for being shoulder to shoulder with me during my time in ARAS; the great contribution we had together is unrepeatable; looking forward to the day we will work together again. Thanks, Farhad, for all the memorable experiences we shared together during undergraduate studies, and afterward, thanks for always being energetic and pushing me forward. Thanks, Mahsa, for providing me with continuous support.

I would like to thank my parents, whose love and guidance are with me in whatever I pursue. To my mother, who has always been a symbol of simplicity and endurance, and to my father, who taught me the meaning of hard work. Many thanks go to my lovely niece Servin; it's because of you that life is beautiful. Most importantly, I wish to thank my loving brother Hamed who was by my side in Canada. Thank you for making me feel at home. Sharing moments of happiness and sorrow has made our bond stronger. Last but indeed not least, I want to thank Marjan. My time in Canada has become more enjoyable with your presence.

In the memory of:

Siavash and Sara

victims of flight PS752

Contents

List of Figures

List of Tables

Nomenclature

Abbreviations

BVP	boundary value problem
CR	continuum robot
CTR	concentric tube robot
DoF	degrees of freedom
HFM	highly flexible member
IK	inverse kinematics
MAE	mean absolute error
MIS	minimally invasive surgery
MRI	Magnetic resonance imaging
PD	proportional-derivative controller
PI	proportional-integral controller
PID	proportional-integral-derivative controller
PRB	pseudo-rigid body
RCM	remote center of motion
RMIS	robotic-assisted minimally invasive surgery

Symbols

α	rotation angle of the flexible part of the hybrid robot
$\boldsymbol{J}_i^T$	ith row of the Jacobian transpose
$\boldsymbol{K}$	Cartesian stiffness matrix
$\boldsymbol{\Delta P}$	vector of the tip point deflection of the HFM
$\boldsymbol{J_d}$	Estimation of the PRB model Jacobian under tip load
$\boldsymbol{\Delta\varphi}^q$	vector of the deflection of the ith joint of the PRB model under qth loading case
$\boldsymbol{\tau}$	vector of the torques at the joints of the PRB model
$\boldsymbol{\varphi}$	vector of the PRB model segment relative angles
$\boldsymbol{J}$	Jacobian matrix of the PRB model
$\boldsymbol{K}_\varphi$	PRB model joint stiffness matrix
$\boldsymbol{l}$	vector of the PRB model segment lengths
$\boldsymbol{p}$	tip position vector of HFM
$\boldsymbol{w}$	wrench vector of the applied force and torque at the tip of HFM
Δx_e	deflection of the environment interacting with the flexible robot
$\Delta\mathbf{x}$	deflection of the robot tip
δx_t	summation of force and position compensations
δx_f	force error compensation
δx_p	position error compensation
ϵ	strain energy of the flexible robot
η	a tuning variable for Jacobian estimation

$\hat{\boldsymbol{p}}$ tip position of vector of the PRB model

$\hat{\theta}_j$ absolute angle of PRB model segments

$\hat{\theta}_{n+1}$ tip angle of the PRB model

$\hat{x}_i$ tip position of the each segment of the PRB model along the X axis

$\hat{x}_n$ tip position of the of the PRB model along the X axis

$\hat{y}_i$ tip position of the each segment of the PRB model along the Y axis

$\hat{y}_n$ tip position of the PRB model along the Y axis

λ Lagrange multiplier

ψ angle of the force with respect to horizontal line

$\mathbf{x}$ tip position of the robot

$\mathbf{x}_d$ desired position of the robot

θ angle of the tangent line at each point along the length of HFM

φ relative angle of ith segments of the PRB model with respect to the adjacent segment

φ^0 relative angle of ith segments of the PRB model with respect to the adjacent segment in no-load condition

φ^q relative angle of ith segments of the PRB model with respect to the adjacent segment under qth loading case

E elasticity module

e position error of the robot tip

E_f force error cost function

e_f force error

E_f^q force error for the qth loading

e_p position error

E_x position error cost function

e_x position error of the PRB model tip point with respect to the continuum model along the X axis

E_x^q position error for the qth loading

e_y position error of the PRB model tip point with respect to the continuum model along the Y axis

e_θ tip point angle error of the PRB model with respect to the continuum model

e_{f_x} force error of the PRB model tip point with respect to the continuum model along the X axis

e_{f_y} force error of the PRB model tip point with respect to the continuum model along the Y axis

e_m tip moment error of the PRB model with respect to the continuum model

EI flexural rigidity

f tip force of the HFM

f_e force applied to the robot tip by environment

g shape function of the HFM

I second moment of area

i number of each joint or the segment of the PRB model

J^T transpose of the PRB model Jacobian matrix

K_e stiffness of the environment

K_i integral controller gain

k_i	stiffness of each PRB model joint
K_p	proportional controller gain
K_r	resultant stiffness of the robot and environment
l_i	length of each PRB model segment
m	bending moment along the length of HFM
m_t	tip moment of the HFM
N	total number of the loading cases
n	DoF of the PRB model
q	number of the loading case
q_1	insertion length of the flexible part of the hybrid robot for eye surgery
q_1	insertion length of the rigid part of the hybrid robot for eye surgery
q_2	rotation angle of the rigid part of the hybrid robot for eye surgery
R	radius of curvature at the tip point of HFM
r	curvature of each point along the length of HFM
S	total length of a HFM
s	position coordinate along the length of HFM
x	position of a each point of the HFM along the X axis
x_n	distance of the base point of the flexible part of the robot with respect to the neutral position of the environment
x_t	tip position of the HFM along the X axis
XY	fixed Cartesian coordinate system

xy	moving coordinate system positioned at the root of the flexible part of the hybrid robot
y	position of a each point of the HFM along the Y axis
y_t	tip position of the HFM along the Y axis
τ_i	torsional force of the ith joint of the PRB model
K_g	geometric stiffness

Chapter 1

Introduction

1.1 Background

Since the advent of minimally invasive surgery (MIS), in the 1980s, surgical interventions techniques in many specialties of the medicine from ophthalmology to pediatric surgery, has been influenced [1]. In MIS, access to the interior organs of the body is provided through small incisions, rather than the large openings in conventional methods. Using a long slender surgical instrument passing through the entry port, the MIS is performed via the far end of the instrument. The advantages of the MIS method are the shortened curing time and hospitalization; less trauma, scarring, and pain; as well as decreased cost of hospital stay, which all benefit the patient. However, the method suffers some drawbacks that mostly impose the surgeon, such as the prolonged learning curve for the surgeons with respect to learning time in open surgery, longer operating time, the non-ergonomic pose of the surgeon, and limited dexterity due to inverted movement of the surgical tool, poor haptic feedback and lack of three-dimensional view of the surgical site [2, 3].

Nevertheless, the integration of surgeon's capability with robotic systems can eliminate the impediment of the MIS method, through increased accuracy, dexterity enhancement, and tremor cancellation. Based on the method, the surgeon can perform the surgical task while teleoperating the surgical robot from a distance in an ergonomic position. Robotic-assisted minimally invasive surgery (RMIS) was first introduced in the early 1990s [4], from then on, it has been an area of extensive research in academia [5, 6, 7, 8], and industry, leading to clinical acceptance of robotic

systems in some surgical operations. Yet, the application of conventional surgical robots, such as da Vinci, is limited to minimally invasive access to the body cavities (e.g., chest or abdomen). Because of the size and delicacy of the eye, the available general-purpose robotic systems are not suitable solutions for vitreoretinal surgery applications, as they are bulky, are not compatible with the size of ophthalmic operating rooms. On the other hand, vitreoretinal surgery requires higher precision compared to other MIS. This limitation has led to the introduction of customized robots for eye surgeries. In conventional eye surgery robots, access to the surgical site is provided through the rotation of a stiff shaft with a tip-mounted instrument about the entry port. Such manipulation of the surgical instrument is generally provided using a remote center of motion (RCM) mechanism. RCM mechanism allows the pure rotation of the payload about a remote point out of the robot structure, which is called the RCM point. Coinciding the RCM point with the entry point of the surgical tool keeps the incision point fixed, which is fundamental in MIS. Fig. 1.1 shows a minimally invasive eye surgery robot introduced by Molaei et al. [9] positioning the instrument in two different configurations.

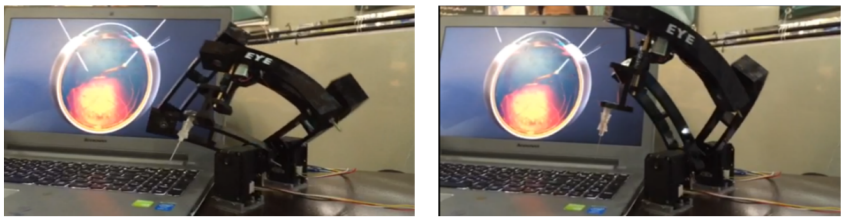

Figure 1.1: DIAMOND eye surgery robot

In vitreoretinal surgery, the rotation of the instrument about the entry port leads to tissue deformation proportional to the thickness of the tissue [10]. Additionally, pivoting the instrument at the entry port limits the dexterity at the tip. In other words, the tip angle of the instrument with respect to the retina cannot be controlled. Due to this limitation, many possible vitreoretinal procedures lack viable MIS alternatives, as they require complex 3-D bends such as intra-vascular navigation. Furthermore, straight instruments increase the risk of collision with the eye lens. Such limitations can be removed by replacing the straight instrument with a continuum robot (CR). It is observed from Fig. 1.2 that CR allows dexterity enhancement and reduces the collision risk with the eye lens

in vitreoretinal surgeries. The shape and structure of a CR are defined by an infinite-degrees-of-freedom (DoF) elastic member, and they can position their tip by flexing along their entire length [11]. Typically, CRs can be constructed at smaller scales than those robots with discrete links due to the simplicity of their structures.

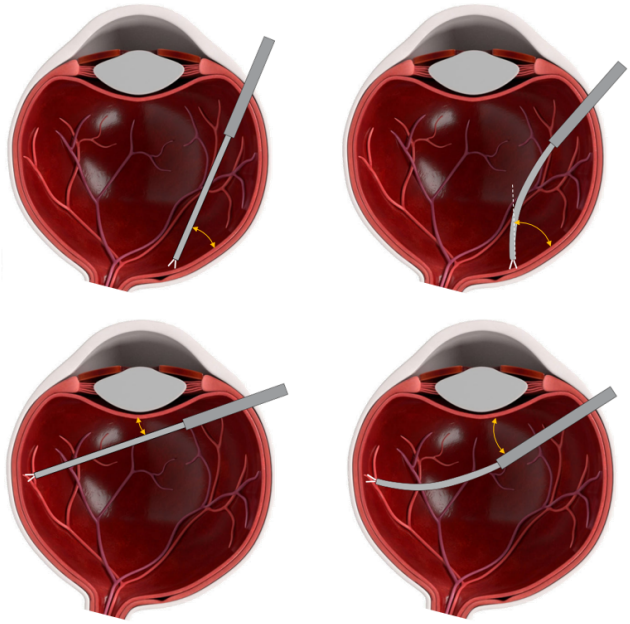

Figure 1.2: Advantages of using CR for dexterity enhancement (top figures) and reducing collision risk with the eye lens (bottom figures)

Two main categories of CRs are backbone CRs and concentric tube robots (CTR). Backbone robots normally have one central elastic structure and series of regularly spaced platforms [12]. By controlling the position and orientation of the platforms using control elements (e.g., cable or wires), the shape of the robot and the position of the distal end of the robot are controlled. On the other hand, a CTR consists of a set of initially-curved, super-elastic tubes, commonly made of nitinol (NiTi), are arranged concentrically in a telescopic way [13]. The elastic equilibrium therefore determines the geometry of the robot of the tubes that shape the structure. In CTR, controlling the relative insertion and rotation of the tubes enable the robot's motion control [14]. Fig. 1.3 Represents the working principles of the two aforementioned CRs.

In recent years, the development of CTRs for use in MIS has become prevalent. CTR has several advantages compared to the backbone ones. They can be designed based on anatomical and surgical

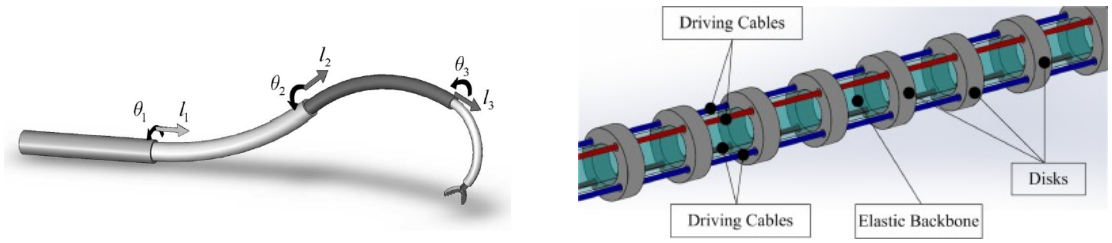

(a) (b)

Figure 1.3: (a) CTR comprising four telescoping HFM that can be rotated and translated with respect to each other. (b) A CR composed of an elastic backbone with equally spaced discs that are controlled via cables

task constraints [15] or patient-specific using 3D printing methods. Thus far, CTRs have been constructed with smaller diameters than many other CRs [12]. As CTRs are the size of a needle, they have a compact structure to be able to navigate through natural orifices. Furthermore, the hollow shaft of the robot can be used to guide control wires for articulated tip-mounted tools [10]. Various medical applications have been proposed for CTRs, e.g., neurosurgery [16], skull base surgery [17], cardiac surgery [18], abdominal surgery [19], urologic surgery [20], and transnasal surgery for orbital tumors [21]. The first application of CTRs for vitreoretinal surgeries was proposed in [22, 23], where a bending tip is included at the tip of a vitreoretinal surgical instrument for dexterity enhancement. It was a hybrid robot comprised of a miniaturized Stewart platform and a 2-DoF CTR with an initially-curved NiTi tube extending from a straight cannula. Later, a 3-DoF CTR was introduced in [24] where the initially-curved tube could rotate within the straight cannula. In another study, a 4-DoF CTR was introduced with two initially-curved tubes, each having two rotational motions and two linear motions with respect to the straight cannula [25]. The proposed robot, anatomy-specific vitreoretinal CTR, is optimized for immobility at the incision and reachability of peripheral retinal regions. As discussed above, replacing CTR with RCM mechanisms brings biomedical advantages increasing the dexterity of clinicians and reducing the risk of a retinal tear, intraocular lens damage, and ocular hypotony [26].

Despite the advantages of CRs, their clinical applications are yet limited due to the complexity of the modeling and control. Compared to the conventional robotic platform, one of the main complexities of CRs arise from the mechanics-based kinematics of the CRs. The kinematics of CRs cannot be described by algebraic equations, and in general, a partial differential equation with

boundary conditions governs the kinematics. This leads to the complexity of the modeling procedure, which is computationally time-consuming, requiring fast algorithms for real-time control applications. Thus, for the simulation and control of the CR, a suitable model should be developed while simple enough to be used for control application and simultaneously having the required accuracy for its application.

Force sensing and control are crucial in robotic surgery to ensure a safe operation. Force feedback is an important factor for patient safety, precise manipulation of soft tissues and improved teleoperation transparency in teleoperation [27]. One advantage of CRs for surgical applications, is their *intrinsic force sensing* [28, 27]. In other words, the shape of the robot can be used as a multi-axis force sensor. This *end-effector as sensor* offers reduced fabrication complexity, increased reliability, sterilizability, MRI compatibility, and further miniaturization, which are practically important [28]. On the other hand, the passive compliance of these robots results in degradation in terms of position accuracy, payload, and force exchange capabilities [29]. The force sensing and force control of CRs is further discussed in the following.

1.1.1 Force sensing in CRs

Force feedback has shown to be an important factor for patient safety, precise manipulation of soft tissues, and improved transparency in teleoperation [27]. In MIS, the surgeon receives force feedback through the distal end of the surgical instruments, which lacks the tactile perception and force cues at the proximal end of the instrument in the surgical site [30]. Similarly, in RMIS, all the natural force feedback is eliminated, which is regarded as a significant limitation of RMIS. Due to this shortcoming, there has been extensive research on the development of surgical robots with force sensing capabilities. The ultimate solution for force sensing would be a miniaturized force sensor at the proximal end of the instrument. However, due to space limitation, sterilization, and MRI compatibility problems, integration of force sensors at the robot tip might not be feasible for specific RMIS procedures. For the case of CRs, the inherent compliance of the robot is regarded as a potential advantage for the force measurement [27]. The concept of intrinsic force sensing of CRs was firstly introduced by Xu and Simman, showing that by the measurement of the actuators load on the multi-backbone CR, certain components of the wrench can be found [27]. Wei and Simaan

presented a unified framework for modeling large deflections of cantilever beams using polynomial approximation and linear interpolation, which can be used for the fast computation of entire robot shape [31]. In [32], Rucker and Webster have addressed intrinsic force-sensing from a probabilistic perspective using an extended Kalman filter. Considering uncertainty in the measurements of the robot's shape and/or end effector pose, they obtained a probability distribution for the external loads on the robot. Tip force estimation of the catheter has been investigated in [33] based on the pose estimation of the tip using a quasi-static catheter model consisting of piece-wise elastic elements. The above discussion shows the uniqueness of the CRs for force control applications, as they provide a safe interaction with the environment and, at the same time, allow us to measure the interaction force with the environment by measuring the deflection of the robot. The focus of this study is the applicability of the CTR for retinal surgery by considering safe interaction via simultaneous force and position control.

In vitreoretinal surgery, surgeons rely on visual feedback for force perception, which is in the order of mN. Based on a previous study, 75% of all forces measured during retinal microsurgery were found to be less than 7.5 mN in magnitude and only 19% of the forces were perceivable by the surgeons [34]. Having force-sensing incorporated in ophthalmic surgical instruments enables quantitative force measurement, preventing undesirable large forces that can damage the retina. Such micron-scale forces are diminished by the friction forces at the entry port of the instrument inside the eye, which requires the force sensor to be integrated at the proximal end of the surgical instrument located inside the eye [35]. In [36], tool with integrated fiber bragg grating sensors, which are placed along with the tool's shaft, is used for the measurement of the tooltip force for membrane peeling in vitreoretinal surgeries. Replacing the rigid instrument with a curved CTR has the benefit of using intrinsic force sensing of CRs, and the tip force can be indirectly estimated through displacement measurement.

1.1.2 Force control of CRs

There are mainly three methods to control interaction forces and motions: stiffness control, impedance/admittance control, and hybrid/parallel force position control. In another classification,

compliant control approaches can be divided into direct and indirect methods. In direct force control, hybrid/parallel force/position control, the force feedback loop is closed by the force controller. However, in the indirect method, impedance/admittance control, the force control is realized through motion control [37]. In stiffness control, the stiffness can be controlled along with all three translations, and the three rotational desired compliance [38] and the controller inputs are a tip configuration set point and the desired stiffness. The problem with the simultaneous control of force and position is that force and position are related, and we cannot control both position and force in the same direction. The impedance control makes the force and position control at the end of the robot equivalent to the "spring-mass-damping" model, and the relation between the force and displacement is controlled.

In the case of retinal eye surgeries, due to high sensitivity, we require higher precision in terms of force, and position control and impedance control strategies are not suitable candidates for such an application. One of the early works in simultaneous control of force and position is that of Raibert and Craig, where the hybrid force/position control is introduced [39]. In force/position control, we cannot control position and force in the same direction simultaneously [40]. The hybrid motion/force control decouples position and force control signals and selects the directions in which the position of the end-effector of a manipulator should be controlled and the directions in which the force exerted by the end-effector should be controlled for a given task [41]. In the parallel hybrid control method, there are two complementary feedback loops, one for the position and the other for the force. The control laws of both loops are added before being sent to the actuator as a global control signal [42]. In addition to hybrid force/position control, external loop force/position control [43] and parallel force position control [44] are two other types of methods that have been used in industry and medical applications. In parallel and external loop force/position control, both force and position are controlled in the same direction while the force controller is prevailing over the position controller, which can be realized by suitable selection of the controller gains.

In CRs, due to the complexity of the mathematical models and the high degree of inaccuracies in modeling, the development of an effective control method is a particularly challenging procedure. Additionally, in the case of miniaturized CRs, integrating a force sensor at the distal end of the robot, which interacts with the environment, is limited. While position control of such flexible

robots has been well covered in the literature, there has been limited attention to the force control problem [45]. Examples of force control for CRs include the stiffness control of CTR presented in [46], force control for single-DoF catheter in [47] as well as hybrid force/position control of multi-backbone CR in [29, 48, 45]. In [29], a hybrid force/position control strategy is introduced for multi-backbone CRs based on the kinetostatic modeling of the CR with a simplified model for robot compliance. In another work, [48] C. Yip et al. have developed a hybrid force/position control for the CR with unknown kinematic and mechanics for cardiac ablation task. The CR in this study is a tendon-driven one with an integrated force sensor at the tip, and the controller also ensures that the tension of the cables remains positive while satisfying the control goal. Smoljkic et al. in [45] have developed a framework for the interaction control of robots featuring large compliance and deformation. In this study, a compliant element is mounted on a serial robotic arm which exhibits large and nonlinear structural compliance, and the proposed framework for the interaction control of the compliance part has been experimentally investigated. Despite the existing literature on the force control of some CRs, for the CTRs, force control is not yet studied [49].

1.2 Problem statement

Complications in vitreoretinal surgery arise from excess and/or incorrect forces applied to the ocular tissue [50]. In vitreoretinal surgery, as discussed, 75% of all forces are less than 7.5 mN in magnitude, and only 19% of the forces are perceivable by the surgeons; thus, surgeons rely on visual feedback for force perception [34]. One common type of vitreoretinal surgery is membrane peeling, in which a thin layer formed on the surface of the retina is removed. Epiretinal membrane is a delicate tissue, and high forces and velocities should be avoided during membrane peeling to prevent damage to the retinal. It has been found that 50% of patients have injuries and defects after membrane peeling because of the high sensitivity of these procedures [51]. By utilizing robotic systems in vitreoretinal surgeries, the surgeon can benefit from higher precision in both positioning and force control. Although simultaneous force control has been investigated in various surgical robots, the force control of CTR is yet to be investigated [49]. To this end, in this study, we investigate a framework to address the force control of CTRs for vitreoretinal surgeries. The robot

under study comprised a 2-DoF CTR mounted on an RCM mechanism, as depicted in Fig. 1.4. The RCM mechanism can orient the CTR about the entry point to the eye $\boldsymbol{O}$. In addition, the insertion length of the concentric tubes can be controlled independently. Using the initially curved CTRs for vitreoretinal surgeries results in dexterity enhancement and safer surgery. Furthermore, we can take advantage of intrinsic force sensing of flexible robots to indirectly measure the force by measuring deflection.

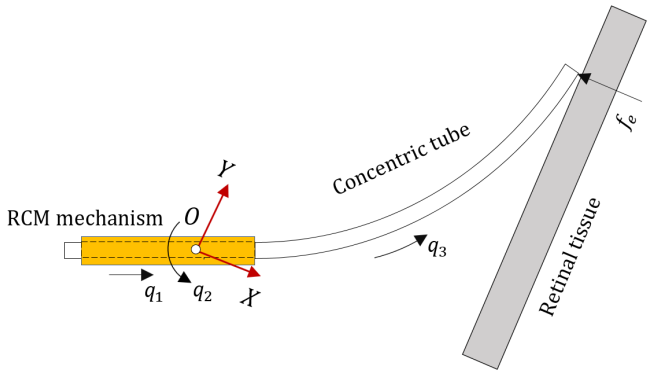

Figure 1.4: Schematic of vitreoretinal surgery using CTR

The simultaneous force/position control of CTR in practice has many challenges that are discussed as follows. First, due to the dependency of the force and position, we cannot have precise control over the force and position in the same direction simultaneously. Furthermore, from the mathematical perspective, the governing equation of the CTR interacting with the environment is a BVP and cannot be used for model-based control designs. In addition, we cannot map the interaction force of the CTR with the environment $\boldsymbol{f}_e$ (which is the desired control force) to that of the joint space torques/forces using the robot Jacobian $\boldsymbol{J}$ via $\boldsymbol{\tau} = \boldsymbol{J}^T \boldsymbol{f}_e$, which is a fundamental mapping in force control schemes. It is because for two reasons: first, in this equation, the strain energy of the CTRs is not taken into account; second, the interaction force with the environment is masked by the large friction forces at the entry port of the robot and also distributed friction force between concentric tubes.

To tackle this problem, we investigate indirect force control methods, where the input to the robot is of type of displacement instead of force/torque in conventional force control schemes. This

requires precise knowledge of the resultant stiffness (Cartesian stiffness) of the robot and the environment at the tip point. The Cartesian stiffness of a robot is defined as the resistance to deformation under external force or torque applied to its end-effector [52], or the tip of the robot in a CR. To the best of the authors' knowledge, the Cartesian stiffness of the CR is yet to be explored. Stiffness formulation becomes more challenging when dealing with initially-curved CTRs with variable lengths. A suitable expression for the robot stiffness can also be used to indirectly measure the force only by knowing the tip deflection. By having the Cartesian stiffness, the compensation force at the task space for the desired force trajectory can be converted to displacement, which can be compensated via kinematic control.

Considering the above discussion, the Cartesian stiffness of the robot is a key role player in the force control of CTR. The Cartesian stiffness of HFM can be modeled using three different methods: virtual joint method, finite element analysis method, and matrix structural method [52]. Since matrix structural and finite element methods are computationally costly, they are unsuitable for real-time applications [53]. Virtual joints utilize the joint space stiffness and Jacobian of the robot to compute the Cartesian stiffness, which can simplify its formulation. However, this method requires joint space stiffness, and finding an accurate joint stiffness is one of the main challenges of this method. To this end, we use pseudo-rigid body (PRB) modeling to obtain an equivalent model of the CTRs. Note that the PRB and virtual joint models use the same concept to find the virtual-joint equivalent of a continuum model. PRB theory is a modeling approach that provides a rigid body equivalent of HFM with large deflections under various loading conditions. Using this method, an HFM can be replaced with n hinged rigid segments with virtual springs at the joints. The PRB model will then be used to formulate the joint space stiffness of the initially-curved variable-length CTRs, which can be used for the Cartesian stiffness model. A 4-DoF PRB equivalent of an initially-curved HFM is depicted in Fig. 1.5, comprised of four rigid segments connected via torsional springs.

1.3 Objectives

In this thesis, we first propose a unified, cost-effective framework for the force-deflection behavior of robots with HFMs using the PRB modeling [25], with CTRs being an example. The highly

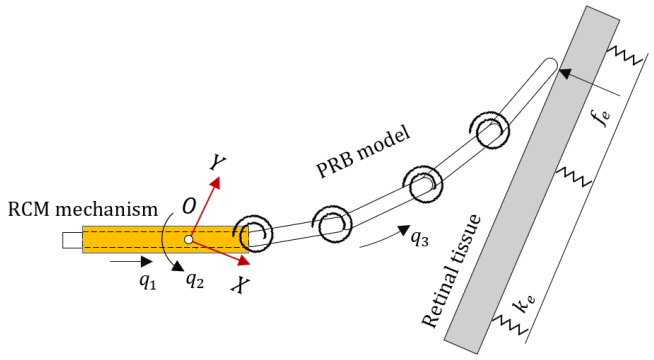

Figure 1.5: Schematics of the PRB equivalent of CTR

flexible members (HFM) are the backbone of flexures, and the outcome of this study can be used by researchers who are not involved with CRs. Flexures are the most common material used for components for high-precision systems, such as nanopositioners and microgrippers. Apart from CTRs, flexures can be found in scanning probe microscopy, lithography, nanometrology, beam steering for optical communication systems, fabrication and assembly of nanostructures, handling and manipulation of micro-objects, micro assembling, machining, and the manipulation of flexible and fragile biological micro-objects such as cells and bacteria in biotechnology [54]. Thus, the proposed approach herein can be used within a wide range of applications in miniaturized applications.

In the PRB modeling approach, the HFM can be modeled via rigid segments connected by virtual torsional springs at the joints. The parameters of the PRB model, the length of the rigid bodies, and the stiffness of the joints are chosen to minimize the cumulative deflection error of the loading at the tip [55] while having similar force/deflection behavior at the same time.

PRB model in CRs has been used for modeling the catheter so far, which has straight geometry. Khoshnam et al. have used a PRB model to analyze planar deflection of catheters [56]. In [57], a PRB model is proposed for an MRI-actuated catheter using 3-DoF PRB model, and the results are experimentally validated. In a recent study, [58] a framework for the 6-DoF continuum manipulators is developed, considering multiple external loads. Using the PRB model for CR modeling is limited to straight-shaped CRs and is not deployed for CTR, which has an initially-curved shape. However, the PRB model for the analysis of curved elastic beams can be found in [59, 60]. In [59], the authors have proposed a 2R PRB model for the circular beam and have extended their model

to a 3R PRB model in [60] with a symmetrical kinematic structure and compliance about the central joint. The symmetrical kinematic and compliance in this study leads to simplification of the optimization problem and computation. However, it limits the number of possible configurations that might have a better result compared to the symmetrical configuration. Secondly, this study is limited to a circular initially-curved beam which, from the practical point of view, is an ideal case for micro-scale manipulation, and it is a fact that any structure goes through deformation in time. Additionally, the optimization problem in the available PRB model literature is done with numerical methods, which lacks analytical insight into the optimization problem. The other shortcoming of the available methods is their limitation for the number of segments as it makes the inverse kinematic complicated, and the existing methods for the PRB modeling of the curved elements are limited to 3-DoF models. Considering the limitations of the available methods for PRB modeling, the first objective of this research is:

First Objective: The first objective of this study will be a versatile PRB modeling approach for the modeling of the initially-curved variable-length CRs having non-uniform stiffness, with no limits on the number of DoF of the PRB model.

By having a suitable PRB model, we can use it for modeling the tip point stiffness of the CR. The stiffness of the robots is defined as the resistance to deformation under external force or torque applied to the robot end-effector [52], or the tip of the robot in CRs. In 1980 Salisbury introduced the concept of the equivalent stiffness of the robots in the task space [38]. In 2000, Chen and Kao showed that the stiffness formulation by Salisbury is only valid in the no-load configurations and introduced an enhanced stiffness model considering the deformation of the robot under the applied load. To the best of the authors' knowledge, the enhanced stiffness is not yet used in the CR field or at least in the CTRs. However, our study shows the enhanced stiffness model, which considers the geometric stiffness, fails to be applied for CRs with large nonlinear deformation. Additionally, the analytical modeling of Cartesian stiffness of the initially-curved CRs with large deflection is an open problem. The Cartesian stiffness is essential in two folds; first, using the Cartesian stiffness, we can estimate the tip force just by measuring the tip deflection; this is specifically important for the case of eye surgery due to limitations for integration of force sensors; secondly, the Cartesian stiffness is essential in the indirect force control schemes to map the force compensation to displacement,

considering the fact that for CTR we cannot map the Cartesian force and moments to the actuators efforts. Regarding the above-mentioned facts, the second objective of our study is:

Second Objective: The second objective of this study will be the formulation of the stiffness analytically for the CRs with an arbitrary pre-curvature, length, and variable stiffness along the length while they have large nonlinear deflection.

In our study, due to the kinematic structure of the CTR and the large friction force, there is no expression to map the tip force to that of the actuators. With this limitation, the available control strategies for simultaneous force/position control cannot be used for the force control of CRs. Additionally, the flexibility of the CRs adds to the complexity of the control problem. Considering the above discussion, the third objective of this research is entitled:

Third Objective: The third objective of this study is to provide a control architecture for the simultaneous force/position control of CR in interaction with a compliant environment.

The indirect force control is based on the fact that the input to the robot is displacement, contrary to the conventional methods, which are force-based. In other words, we indirectly control the force via position input. To verify the effectiveness of the proposed control architecture, we have developed a continuum model for the interaction of the robot with the environment, and the controller is applied to the continuum model.

1.4 Thesis Contribution

The main contribution and novelties of this research are:

(1) Using simple PID controllers, a novel method for the hybrid force/position control of initially-curved variable-length CR with arbitrary stiffness along the length. To the best of the authors' knowledge, the force control of the CTR is yet to be demonstrated [49], which is due to two main facts.

   (a) The governing equation of the CR in contact with the environment is a boundary value problem (BVP) and is not suitable for the model-based control design.

   (b) Distributed contact forces between the tubes along their length and the concentrated

bending moments generated at discontinuities in curvature and at the boundaries generate friction forces [61]. On the other hand, there are also unknown friction forces at the entry point of the robot for vitreoretinal surgeries. Thus, the existing formulation for the static force mapping for CRs is not accurate [49].

(2) A versatile semi-analytical method for PRB modeling of HFM with the following novelties and advantages compared to conventional approaches:

   (a) It has an analytical insight into the PRB modeling problem.

   (b) Can Directly provide PRB model for arbitrarily curved HFM, including CRs.

   (c) It can be used for PRB modeling of initially-curved HFMs with variable stiffness.

   (d) The complexity of inverse kinematics, which was the burden of the PRB method, is removed, and the method can be used for PRB modeling with arbitrary DoF.

   (e) The proposed method can be used for the PRB model of variable length HFM, which can be found in CTR applications.

   (f) The proposed method can be simply used by researchers in robotics, continuum mechanics, compliant mechanisms, etc., due to the simplification of the PRB method thanks to the proposed method.

(3) An analytical approach for finding the deformed shape of HFMs only through tip deflection measurement using the PRB model of the HFM.

(4) A highly accurate method to measure the tip force of the HFM is merely by measuring the tip deflection using the PRB model of the HFM. The advantages of the proposed approach are two folds:

   (a) It is an indirect way of force measurement which removes the barriers of integrating the force sensor at the tip of the robot.

(b) With the proposed method, one can measure the interaction force of the robot with the environment just by measuring the tip deflection using imaging techniques or magnetic sensors out of the surgical site.

(5) An analytical expression for the Cartesian stiffness of CRs. The importance of this contribution can be better explained as being the first method in the literature that offers an analytical expression of the Cartesian stiffness of CRs.

(6) Development of a BVP model which describes the interaction of the an initially curved HFM with a compliant environment.

1.5 Thesis Layout

Chapter 2 starts with the quasi-static modeling of HFM in the general form under combined force and moment loading at the tip. Then we discuss the existing methods for PRB modeling of the HFMs in detail and their shortcomings. Discussing the limitation of the literature in the field for the modeling of the variable-length initially-curved and non-uniformly stiff HFM, we propose a versatile semi-analytical methodology for the PRB modeling. The versatility of the proposed method is then investigated in five case studies in CRs. Chapter 3 is devoted to the stiffness modeling of the HFM under pure force loading at the tip based on the PRB model developed in Chapter 2. In this chapter, first, we discuss the existing methods for modeling the stiffness. Our studies have shown that the existing methods fail to be applied to the HFMs, which have large deformations under the applied load. On the other hand, the more accurate existing stiffness formulation, referred to enhanced stiffness model, is based on knowing the force and cannot be applied in our application. Considering the limitation of the existing method, we develop a novel formulation for the stiffness of the HFM as a function of tip point deflection. The validity of the proposed formulation is compared to the existing method at the end of the chapter for an initially-curved CR. Additionally, we propose a new formulation for estimation of the deformed shape of the HFM under pure tip loading, just by knowing a single point deflection. The validity of the proposed method is then compared with the PRB model deformation. Chapter 4 is devoted to controller design for CRs, using the findings

of the previous two chapters. In this chapter, first, we formulate the interaction of CRs with a compliant environment. Looking into the formulation of the problem and considering the practical implementation, we discuss the constraint of the control problem. Then we provide a suitable control strategy for the simultaneous force and position control of CRs. As the existing methods are based on the force input to the robot, considering the formulation of the problem and the practical constraint, they cannot be applied to control CR. Thus, we proposed a modified version of the existing methods as potential candidates for control. Finally, we design a control architecture for the indirect hybrid force/position control of the CRs. The tracking performance of the proposed control architecture is then evaluated at the end of this chapter for two scenarios. The thesis is finalized by summarizing the research outcome and discussing the future works in Chapter 5.

Chapter 2

Pseudo-Rigid Body Modeling

2.1 Background

Highly flexible members (HFM) have been extensively used in the design of mechanical systems where the force characteristic of the system is essential. Such a kind of application can be found in compliant mechanisms to design constant force grippers [62], in robotic fish fin to maximize the trust [63], continuum robots (CR) for surgical applications [64], as well as micro-manipulation devices [65]. Additionally, they have a pivotal role in the realm of microorganisms and biomimetic robotics, and as we go down the dimension, the compliant structure reigns [66]. Flexural elements in robots are slender beams that undergo large nonlinear deformation under external loads. These elements can be used as the joint or the linkages of the robots, which helps eliminate problems related to bearing friction or wear and tear and backlash. Additionally, they can be used to design robots that can be fabricated as a single system, eliminating the need for assembly [67]. On the other hand, having an optimal design for flexible elements to replicate biological properties in robots allows robots to use natural dynamics, reduce energy demand, enhance mechanical performance, safety, and efficiency [68]. Moreover, mechanical compliance increases safety in human-robot co-operation by absorbing some kinetic energies, reducing the impact on the human operator [69]. Furthermore, flexural bodies are suitable for morphological adaptation to complex environments for surgical operations to guide through body cavities into the surgical site while minimizing damage to the body [70]. While having significant advantages in performance, flexural elements in robots

limit applying the existing methods for rigid body robotics in design, analysis, and control. In these elements, the kinematic is not just a geometric problem and is influenced by actuation and external loading [71]. Thus, the kinematic analysis requires a model of the HFMs' nonlinear deformation described by a two-point BVP. The analysis of flexural elements deformation has been studied using the finite element method [72], the Pseudo-rigid body (PRB) model, and the Cosserat rod theory, among others.

PRB theory is a modeling approach that provides a rigid body equivalent of HFM with large deflection under various loading conditions. Using the PRB modeling method, a HFM can be replaced with n hinged rigid segments with virtual springs at the joints, and n, in fact, is the degrees-of-freedom (DoF) of the PRB model. Thus, the force-deflection behavior of the HFM can be obtained using algebraic equations through the PRB model, which is primarily a boundary value problem (BVP) in the continuum representation. From the mathematical perspective, a PRB equivalent model of a continuum element can be formulated as an optimization problem, where the optimal values for the segment lengths and the stiffness of the virtual springs are to be found. This is done by formulating the static force mapping of the PRB model using its Jacobian matrix. This formulation, however, requires the deformation of the virtual springs. Thus, the tip deflection under a given tip load, found using the continuum model, can be used to formulate the inverse kinematics (IK) for finding each virtual spring deformation. This implies that the PRB model is formulated as a two-objective optimization problem, which should satisfy the static force mapping over a range of loads, and at the same time, should meet the IK. By increasing the DoF of the PRB model, the problem of finding optimal parameters of the PRB model becomes more complex, as there is no unique analytical formulation for the IK of the serially hinged rigid segments with a DoF greater than three.

Larry L. Howell first introduced the PRB theory in 1994 as an approximation technique for modeling a compliant/flexure mechanism [73] and has been used for modeling robotics systems made of HFM in various applications. The simplicity of the PRB model makes it an ideal alternative for the continuum model and finite element model of HFMs from the computational perspective [74]. In [74], the computation time of the PRB model is compared to that of the finite element approach for a single static loading. The simulation is performed on a 64-bit Intel Xeon computer with 112

GB memory at 2.40 GHz. It was observed that the computation time of the PRB model was less than 0.1 seconds, while it was 17 seconds for the finite element method. A PRB equivalent model allows well-developed methods in rigid robotics to be applied to robots with flexible elements. Applications of this modeling approach can be found in a robotic fish, where the optimal compliance of the fish fin is determined for maximizing the thrust [63]. In [75], the PRB modeling method is used for a robot with inflatable links. In another study [76], this method is used for analyzing and designing an avian-inspired passive perching mechanism for a robotic rotorcraft. This method has also been used to model a new insertable robotic end-effectors platform for single port surgery [64]. The simplicity of the PRB model, compared to the continuum model, makes it an efficient method for modeling CRs. That is why several researchers in this area have recently used it. The authors in [77] use the method for modeling fiber-reinforced elastomeric enclosures that are fundamental building blocks of pneumatic soft robots. The work in [56] employs a 3-DoF PRB model to model catheter tip force for the control purpose. In another work, the authors in [58] use this method to study the deformed shape and reaction forces of continuum manipulators interacting with their environment and verify it experimentally. In [78], the 3D static modeling method and experimental verification of CRs based on PRB theory have been investigated. The authors in [79] use this method to investigate the kinematics of MRI-compatible, magnetically actuated, steerable catheters, and the experimental results are provided in [57]. The work [79] also introduces a method of finding a set of parameters for the PRB model from a set of experimental data for the catheter. The authors in [80] use the PRB model of an MRI-actuated CR for the quasi-static Jacobian-based task space motion planning. The PRB model has also been used in a recent study in needle steering for adaptive energy shaping control [81].

The PRB modeling method was initially developed for HFMs subjected merely to end moment [82] or to end forces [83], assuming the tip of the HFM follows a circular path. Parametric approximation of the straight HFM tip deflection using the PRB modeling method started with a 1-DoF model consisting of two rigid links hinged with a torsional spring, which had large error values for large tip deflection angles [83]. The accuracy of the PRB modeling method was improved in [84], using a 3-DoF model with a maximum tip deflection error of 1.2% compared to the finite

element model. The authors in [85], formulated the problem in the particle swarm optimization context with the methodology introduced in [84] to increase the precision. The PRB modeling method has also been utilized to analyze the circular HFM [59, 60]. In [59], a 2-DoF PRB model is proposed for the circular HFM with an error not exceeding 3.05% in the tip position. The method is then extended to the 3-DoF PRB model in [60] with a symmetrical kinematic structure and compliance about the central joint for a circular HFM with a uniform cross-section.

As the existing PRB modeling methods are formulated for specific case studies, the limitations of these methods cannot be identified. To better understand the shortcoming of the PRB modeling in literature, we have generalized a recent PRB modeling formulation introduced in [60]. This method offers a 3-DoF PRB model for constant curvature, uniformly-stiff HFM, assuming symmetrical length and stiffness around the central joint, to simplify the problem. Our extended formulation (see Algorithm 1) considers an n-DoF PRB model for arbitrary-curved HFM with nonuniform stiffness along the length. Considering Algorithm 1, the limitations of the existing methods are as follows.

It requires the IK solution for the PRB model, which does not have a unique analytical solution for a DoF of more than three. Consequently, most of the existing methods for the PRB modeling are developed for 3-DoF, which limits the precision of the PRB model. The higher the DoF, the higher the precision of the model [84]. Additionally, the initial position of the joints in the no-load condition should be specified, which is supposed to satisfy the equation representing the centerline of HFM. This assumption will be formulated as multiple equality constraints in the optimization problem. Moreover, the existing formulation requires additional constraints on the positiveness of the stiffness and length of the elements with proper upper bounds. More importantly, the resultant optimization problem involves, in general, a two-objective, highly nonlinear equation that is to be solved numerically. One other shortcoming of the existing methods in the literature is that there is no direct method for the PRB modeling of initially-curved HFMs with arbitrary curvature to the best of the authors' knowledge. Such modeling is generally done by dividing the variable curvature HFM into circular segments and finding the PRB model for each circular segment. One reason behind this limitation is the complexity of the initialization of the joint position in the no-load condition. For HFMs with a circular shape, the length of each rigid segment of the PRB model is equal to the cord of a circle which is a fraction of the total angle of the circular HFM. However, for an arbitrary curve,

the length of the segment cannot simply be determined, which leads to a complex set of nonlinear equations. Furthermore, there is no unified, comprehensive method that can be used for the general PRB modeling problem, and most of the studies are limited to specific case studies such as straight HFMs. Moreover, there are applications, such as concentric tube robots (CTR), in which the length of the HFM changes. The available methods fail to cover such applications suitably.

To overcome the shortcomings of the existing literature discussed, we propose a novel methodology for quasi-static PRB modeling, which can easily be used in various applications. In the proposed method, the BVP corresponding to the quasi-static continuum model, which is used only to find the tip deflection in the existing methods, is used to solve the IK. As a result, the two cost functions are decoupled, and the optimization problem in PRB modeling becomes a single objective specified by the static force mapping equation. Then we propose an analytical solution to the optimization problem, which provides the optimal values of stiffness of the virtual springs for an n-DoF PRB model. Through different case studies, we show how the proposed method can be used for initially-curved CRs with variable stiffness along the length for both constant and variable lengths. The results of our studies also provide an n-DoF PRB model for arbitrarily curved uniformly stiff HFM with just three parameters.

In the following, first, the Euler beam theory for the general case of HFM is formulated in Section 2.2,. In Section 2.2, we provide a general formulation for the PRB modeling. Then in Section 2.3, the proposed methodology is described in detail. Next, in Section 2.4, the application of the proposed method is investigated for five different case studies, considering straight, circular, arbitrarily initially-curved, and non-uniformly-stiff, as well as variable-length HFMs. As illustrated in Fig. 2.1, the PRB model will result in a diagonal stiffness matrix $\boldsymbol{K}_{\varphi}$, which will be used in the following chapter for the Cartesian stiffness model of slender CRs.

2.2 Force/deflection Modeling of HFMs

An initially curved HFM defined by $\theta(s)$ with the total length of S under the applied force f and moment m_t is demonstrated in Fig. 2.2. The other end of the HFM is clamped, such that $\theta(0) = 0$. This condition is valid at the contact point of the catheter with the arteries and the exit point of

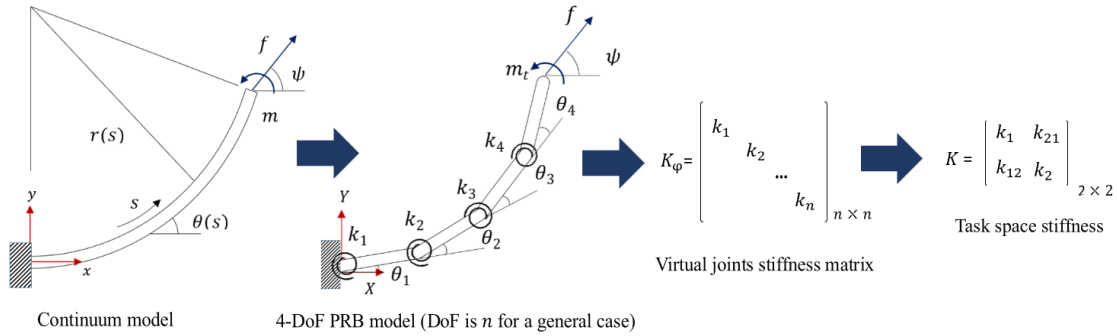

Figure 2.1: The proposed methodology for obtaining Cartesian stiffness model of slender CRs

initially-curved inner tubes in CTRs. The HFM has a no-load curvature $r(s)$ along the length. The stiffness of the HFM, referred to as flexural rigidity, is a function obtained by multiplication of the elasticity module E of the material and the second moment of area I; either of them could change along the length. For generality, we represent variable flexural rigidity as a function of length defined by $EI(s)$ and constant flexural rigidity by EI. As the deformation of the HFM is mainly

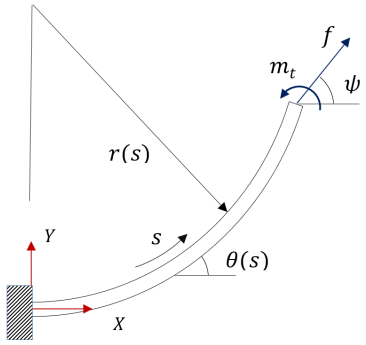

Figure 2.2: An initially curved HFM with a load at the tip

due to the shear moment, the Euler beam theory suitably describes its behavior. With an applied load at the tip, the bending moment $m(s)$ along the deformed HFM is given by:

$$\begin{cases} m(s) = m_t + f(x_t - x)\sin\psi - f(y_t - y)\cos\psi \\ x(s) = \int_0^s \cos\theta(\xi)d\xi \\ y(s) = \int_0^s \sin\theta(\xi)d\xi \end{cases} \tag{2.1}$$

where $\boldsymbol{p} = [x_t, y_t, \theta_t]$ represents the tip position vector of the continuum model, and ξ is the integral variable. The shape of the HFM under the applied load at the tip can be expressed using the Euler beam theory as:

$$\theta'(s) = \frac{m(s)}{EI(s)} + \frac{1}{r(s)} \tag{2.2}$$

Using Eq. (2.1) and differentiating (2.2) with respect to s results in:

$$\begin{cases} \theta''(s) = \frac{m'(s)}{EI(s)} - \frac{EI'(s)m(s)}{EI^2(s)} - \frac{r'(s)}{r^2(s)} \\ m(s) = m_t + f(x_t - x)\sin\psi - f(y_t - y)\cos\psi \\ x(s) = \int_0^s \cos\theta(\xi)d\xi \\ y(s) = \int_0^s \sin\theta(\xi)d\xi \\ \theta'(S) = \frac{m(S)}{EI(S)} + \frac{1}{r(S)} \\ \theta(0) = 0 \end{cases} \tag{2.3}$$

Equation (2.3) is the general governing equation of a 2D HFM under tip load. This can be used for the modeling of a HFM which has variable curvature and variable stiffness along the length. When dealing with constant curvature $r(s) = R$ and uniform stiffness, Eq. (2.3) is simplified as:

$$\begin{cases} \theta''(s) = \frac{f}{EI}\sin(\theta - \psi) \\ \theta'(S) = \frac{m(S)}{EI} + \frac{1}{R} \\ \theta(0) = 0 \end{cases} \tag{2.4}$$

Note that Eq. (2.3) is computationally complex, in general. This is important for real-time control of flexible robots interacting with a soft environment. Additionally, force control schemes require the knowledge of the Cartesian stiffness of the robot [86, 87, 46], which cannot simply be obtained using Eq. (2.3). By using a PRB model, the formulation of the Cartesian stiffness of the robot is simplified. Additionally, the stiffness model can estimate the interaction force via deflection measurement.

For the PRB modeling of a curved HFM with a total length of S, it is first divided into a finite

number of rigid segments. An n-DoF PRB model generally includes n rigid segments connected via n revolute joints with torsional springs. The stiffness of each revolute joint is represented by k_i, and the length of each segment is l_i for $i = 1 : n$. We use $\boldsymbol{K}_\varphi$ as the diagonal matrix of the joint stiffness $diag(k_1, ..., k_n)$ and $\boldsymbol{l}$ as the vector of the segments' length, i.e. $[l_1, .., l_n]^T$. Fig. 2.3 shows a 4-DoF PRB model connected to a base via a torsional joint. In this figure, the relative angle

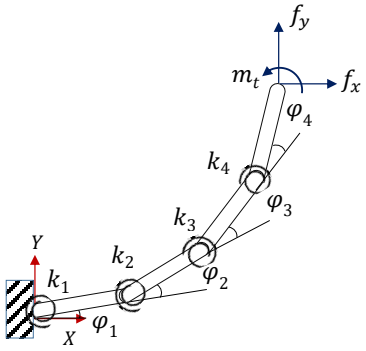

Figure 2.3: A 4-DoF PRB model of a curved HFM

of each segment with respect to its adjacent segment is denoted by φ_i, with $\boldsymbol{\varphi}$ being the vector of joint variables, i.e. , $[\varphi_1, ..., \varphi_n]^T$. Note that φ_1 is measured with respect to the horizontal line. Introducing $\hat{\theta}_j = \sum_{i=1}^{j} \varphi_i$ for $i = 1 : n + 1$ as the angle of each segment with respect to the horizontal line, the tip position of each segment with respect to the fixed Cartesian frame, depicted in Fig. 2.3 can be written as:

$$\begin{cases} \hat{x}_i = \sum_{j=1}^{i} l_j \cos \hat{\theta}_j \\ \hat{y}_i = \sum_{j=1}^{i} l_j \sin \hat{\theta}_j \end{cases} \tag{2.5}$$

Notably, we use $\hat{}$ to differentiate between the variables in the continuum and PRB model. Moreover, as there is no joint at the tip, we refer to the tip angle of the PRB model by $\hat{\theta}_{n+1}$ by considering a virtual segment with a zero length. Using the above formulation, the tip position vector $\hat{\boldsymbol{p}}$ of the PRB model, i.e. $[\hat{x}_n, \hat{y}_n, \hat{\theta}_{n+1}]^T$, is expressed by:

$$\begin{cases} \hat{x}_n = \sum_{j=1}^{n} l_j \cos \hat{\theta}_j \\ \hat{y}_n = \sum_{j=1}^{n} l_j \sin \hat{\theta}_j \\ \hat{\theta}_{n+1} = \sum_{i=1}^{n+1} \varphi_i \end{cases} \tag{2.6}$$

with φ_{n+1} being a constant offset value, which is the difference of the tip angle of the continuum model and the PRB model in the no-load condition.

Let the applied wrench at the tip ($\boldsymbol{w} = [f_t \cos\psi, f_t \cos\psi, m_t]^T$) be mapped to the torsional force of the virtual springs ($\boldsymbol{\tau} = [\tau_1, ..., \tau_n]^T$) at the joints using the Jacobian matrix ($\boldsymbol{J}$) as:

$$\boldsymbol{\tau} = \boldsymbol{J}^T \boldsymbol{w} \tag{2.7}$$

Each element of $\boldsymbol{\tau}$ in the above equation is proportional to the deflection of the corresponding joint $\delta\varphi_i$ under the applied load, i.e., $\tau_i = k_i \delta\varphi_i$. This can be written in the matrix form as $\boldsymbol{\tau} = \boldsymbol{K}_{\boldsymbol{\varphi}} \boldsymbol{\Delta\varphi}$, with $\boldsymbol{\Delta\varphi} = [\delta\varphi_1, ..., \delta\varphi_n]^T$. On the other hand, the Jacobian matrix is by definition, expressed as $\boldsymbol{J} = \partial\hat{\boldsymbol{p}}/\partial\boldsymbol{\varphi}$. For an n-DoF PRB model, using $\hat{x}_i$ and $\hat{y}_i$ as defined in Eq. (2.5) the Jacobian can be expressed by:

$$\boldsymbol{J}_{3\times n} = \begin{bmatrix} -\hat{y}_n & ... & -(\hat{y}_n - \hat{y}_i) & ... & -(\hat{y}_n - \hat{y}_{n-1}) \\ \hat{x}_n & ... & (\hat{x}_n - \hat{x}_i) & ... & (\hat{x}_n - \hat{x}_{n-1}) \\ 1 & ... & 1 & ... & 1 \end{bmatrix} \tag{2.8}$$

2.2.1 Parameter Optimization of PRB Model

It is now desired to derive a PRB model analogous to that of a continuum model with the highest accuracy in describing the tip point displacement and the compliance behavior under a wide range of loads. This constitutes an optimization problem which can be expressed by two sets of cost functions, $E_f = \frac{1}{N}\sum_{q=1}^{N} \|\boldsymbol{K}_{\boldsymbol{\varphi}}\boldsymbol{\Delta\varphi} - \boldsymbol{J}^{\boldsymbol{T}}\boldsymbol{w}\|^q$ and $E_x = \frac{1}{N}\sum_{q=1}^{N} \|\boldsymbol{p} - \hat{\boldsymbol{p}}\|^q$, for the force and position errors; in which q represents each loading condition with a specific wrench ($[f_x, f_y, m_t]^q$) and N is the total number of the loading conditions. We represent the no-load condition $\boldsymbol{w} = \boldsymbol{0}$ with $q = 0$. In this optimization problem $\boldsymbol{\Delta\varphi^q}$ is the optimization variable and $\boldsymbol{l}$ and $\boldsymbol{K}$ are the unknown parameters. The $\boldsymbol{\Delta\varphi^q} = \boldsymbol{\varphi}^q - \boldsymbol{\varphi}^0$, requires $\boldsymbol{\varphi}^q$ and $\boldsymbol{\varphi}^0$, which are obtained through the IK solution of the PRB model in each loading condition and its no-load configuration, respectively. On the other hand, $\hat{\boldsymbol{p}}$ and $\boldsymbol{J^T}$ are defined as functions of $\boldsymbol{\varphi}^q$, $\boldsymbol{\varphi}^0$ and $\boldsymbol{l}$, i.e. $\hat{\boldsymbol{p}} = \hat{\boldsymbol{p}}(\boldsymbol{\varphi}^q, \boldsymbol{\varphi}^0, \boldsymbol{l})$ and $\boldsymbol{J^T} = \boldsymbol{J^T}(\boldsymbol{\varphi}^q, \boldsymbol{\varphi}^0, \boldsymbol{l})$. Generally, for the curved HFMs as in [60], it is assumed that in the no-load

condition, the joints of the PRB model lie on the centerline of the continuum model curve. The centerline of the curve is a continuous function of x and y which can be defined as $g(x, y) = 0$. This assumption works as an additional constraint, such that the relation of $g(\hat{x}_i^0, \hat{y}_i^0) = 0,\ i = 1 : n$ holds in the optimization procedure, in which $(\hat{x}_i^0, \hat{y}_i^0)$ represents the no-load position for each of the PRB model joints. The equation representing function $g(x, y)$ could be complex, in generalNote that the length of the segments l_i and stiffness of the joints k_i cannot have negative values for physical systems. Thus, the optimization problem for the PRB modeling of initially-curved HFMs can be formulated as follows:

$$
\begin{cases}
E_f = \frac{1}{N}\sum_{q=1}^{N} \|\boldsymbol{K_\varphi \Delta\varphi} - \boldsymbol{J^T w}\|^q \\
E_x = \frac{1}{N}\sum_{q=1}^{N} \|\boldsymbol{p} - \hat{\boldsymbol{p}}\|^q \\
k_i > 0,\ l_i > 0 \\
\begin{cases}
\hat{\boldsymbol{p}}^q = [\hat{x}_n^q, \hat{y}_n^q, \hat{\theta}_{n+1}^q]^T \\
\boldsymbol{p}^q = [x_t^q, y_t^q, \theta_t^q]^T \\
\hat{x}_n^q = \sum_{j=1}^{n} l_j \cos\hat{\theta}_j^q \\
\hat{y}_n^q = \sum_{j=1}^{n} l_j \sin\hat{\theta}_j^q \\
\hat{\theta}_j^q = \sum_{i=1}^{j} \varphi_i^q
\end{cases} \\
\begin{cases}
g(\hat{x}_i^0, \hat{y}_i^0) = 0 \\
\hat{x}_i^0 = \sum_{j=1}^{i} l_j \cos\hat{\theta}_j^0 \\
\hat{y}_i^0 = \sum_{j=1}^{i} l_j \sin\hat{\theta}_j^0 \\
\hat{\theta}_j^0 = \sum_{i=1}^{j} \varphi_i^0
\end{cases}
\end{cases}
\tag{2.9}
$$

Due to the strong coupling of the cost functions E_f and E_x to the IK, for simplicity, most of the existing results in the literature consider 3-DoF PRB models. Note that for an n-Dof PRB model with N loading conditions, $n(N+2)$ unknowns are to be found, e.g., more than 3 million unknowns for a 100-DoF PRB model over 3000 loading conditions. As discussed, the optimization problem, defined by Eq. (3.10) also requires the IK for the no-load condition, and due to its complexity,

merely the circular or straight HFMs are studied in the literature such as [60]. In the above work, it is also assumed that the first and the third joint have the same stiffness and length, i.e., $k_1 = k_3$ and $l_1 = l_3$, which limits the search algorithm.

From the above discussion and Eq. (3.10) finding an arbitrary n-DoF PRB model, in general, is a complex problem. Therefore, the PRB modeling methods in the literature are limited to constant-curvature HFMs with uniform stiffness distribution along the length with limited DoF. Furthermore, most existing methods have moderate accuracy, which may not be acceptable in many medical applications. Algorithm 1 describes the formulation discussed above for the PRB modeling. In the next section, we propose a different yet straightforward semi-analytical approach to overcome the shortcomings. It is to be noted that $\boldsymbol{p}$ in Algorithm 1 can also be obtained directly through experiment.

Algorithm 1 General method for the PRB modeling of HFMs

initialize $S > 0$, $EI(s)$, $r(s)$, and $N, n \in \mathbb{N}$
$g(x, y) \leftarrow$ use $r(s)$
Require: w_q for $q = 1 : N$, ▷ w_qs should cover the actual loading conditions of the HFM
symbolically formulate $\hat{\boldsymbol{p}}$ as a function of $\boldsymbol{l}$ and $\boldsymbol{\varphi}$ using (2.5)
symbolically formulate $\boldsymbol{J}$ for the n-DoF PRB model using (2.8)
symbolically fromulate $\boldsymbol{\varphi}^0$ as a function of $\boldsymbol{l}$ using g
for $q = 1 : N$ **do**
    $\boldsymbol{p} \leftarrow$ solve (2.3) for $\boldsymbol{w}_q = [f_t \cos\psi, f_t \sin\psi, m_t]^T$
    $E_f^q = \|\boldsymbol{p} - \hat{\boldsymbol{p}}\|^q$
    $E_p^q = \|\boldsymbol{K}\boldsymbol{\Delta}\boldsymbol{\varphi} - \boldsymbol{J}^{\boldsymbol{T}}\boldsymbol{w}\|^q$
end for
$E_p = \frac{1}{N}\sum_{q=1}^{N} E_f^q$
$E_f = \frac{1}{N}\sum_{q=1}^{N} E_f^q$
Set the constraints as: $k_i > 0$ & $l_i > 0$ & $\sum_{i=1}^{n} l_i \leq s$
Minimize E_p & E_f and find the optimal θ_i^qs, k_is and l_is

2.3 A Versatile PRB Modeling Framework

The main idea behind the proposed approach herein is to decouple the IK from the optimization procedure. Thus, the values of $l_1, ..., l_n$ are first found, and subsequently, the optimal stiffness $k_1, ..., k_n$ associated with them are obtained analytically using E_f. To this aim, we use Eq. (2.10) for solving the IK, which describes the mechanical behavior of HFMs under tip loading. This approach results in realistic values for optimization variables compared to the existing methods,

which formulate IK with a geometric equation without capturing the physical behavior of HFMs. Additionally, in our method, as the physics is included in the IK formulation, the behavior of the PRB model along the length is also close to the realistic behavior. It is in contrast with the existing methods, where the PRB model is obtained just by matching the displacement of the tip point with that of the continuum model, and deflection of the HFM along the length is not considered. In the proposed approach, first, the DoF of the PRB model n is chosen. It is to be noted that there is no limit on the maximum value of n in the proposed method. The larger the n, the higher the precision of the method. Secondly, we divide the length of the HFM into n segments $[s_1, ..., s_n]$, which results in $n+1$ points along the curve length. Then, the governing continuum equation of the HFM is numerically solved for the given load, while the curve is divided into n segments, where the length of segment $i = 1 : n$ is s_i. As the first step of the proposed method, we let $s_i = l_i$. In other words, the length of each segment of the PRB method is specified, which is the first step in solving the IK. Solving the inverse kinematic for the PRB model also requires the angle of each segment. To this end, we introduce a new representation of the deformation of the HFM, which is represented in the length coordinate by Eq. (2.3) in Cartesian coordinates. This is done by incorporating x and y with the corresponding boundary conditions in Eq. (2.3), which results in Eq. (2.10).

$$\begin{cases} \theta''(s) = \dfrac{m'(s)}{EI(s)} - \dfrac{EI'(s)m(s)}{EI^2(s)} - \dfrac{r'(s)}{r^2(s)} \\ x'(s) = cos\theta(s) \\ y'(s) = sin\theta(s) \\ \theta(0) = x(0) = y(0) = 0 \\ \theta'(S) = \dfrac{m(S)}{EI(S)} + \dfrac{1}{r(S)} \end{cases} \tag{2.10}$$

By solving the above equation with BVP solvers for the $n+1$ points along the length, one can find the corresponding $(\hat{x}_i, \hat{y}_i)$. Thus, the absolute angle of each segment $\hat{\theta}_i$ is found using the following equality:

$$\hat{\theta}_i = \arctan(\frac{\hat{y}_i - \hat{y}_{i-1}}{\hat{x}_i - \hat{x}_{i-1}}),\ i = 1 : n \tag{2.11}$$

Using Eq. (2.10) for the IK ensures that the absolute value of the position error (E_x) is minimized, and at the same time, E_f is decoupled from E_x. Thus, the optimization of the PRB model requires minimizing E_f. For a better insight into the working principle of the proposed method for minimizing E_x, we consider an initially-curved HFM under a loading condition, resulting in large deflection. The HFM used in this simulation study is the inner tube of a CTR, with the parameters specified in Table 2.4. The simulation is done for a loading condition, 100 mN in magnitude, applied at the tip with the angle of 156° with respect to the horizontal plane. For the given load, we have compared the shape of the continuum model and the PRB models with 3, 4, 10, and 30-DoF in Fig. 2.4.

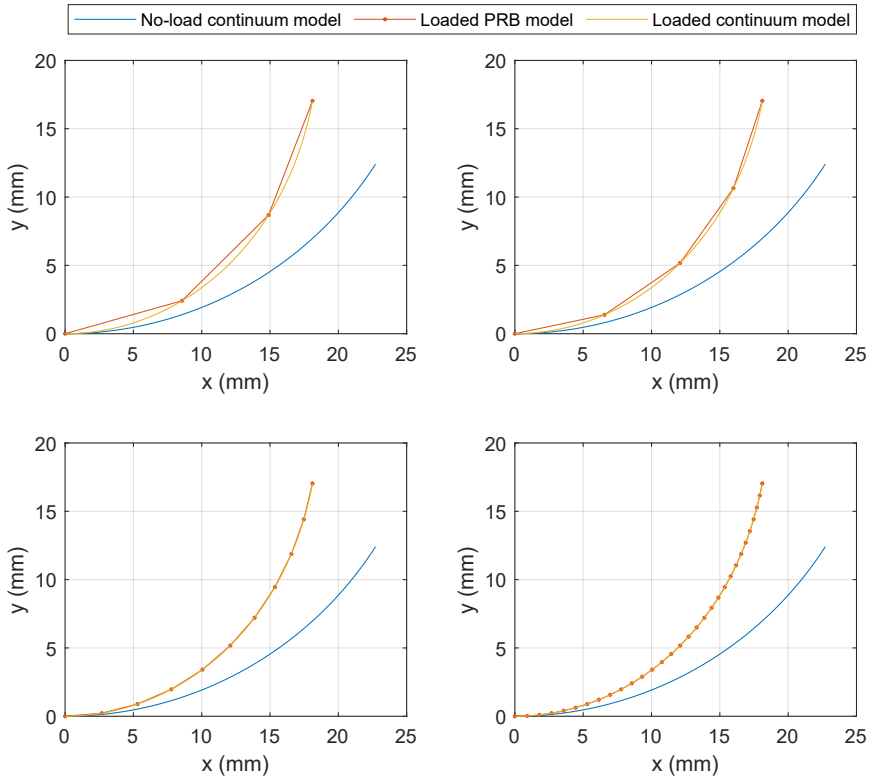

Figure 2.4: Deformation of the continuum model compared to the PRB models with 3, 4, 10 and 30-DoF

As observed from the above figure, all the PRB models suitably capture the deflection of the continuum model along the length. For a better comparison, the normalized mean absolute error (MAE) for the tip position is also given in Table 2.1. The results confirm a higher precision for larger DoFs.

Table 2.1: Normalized MAE of the PRB models' tip position compared to that of the continuum model

DoF	3	4	5	30
MAE $\times 10^{-4}(\%)$	0.2952	0.0508	0.0006	0.0001

In the following we investigate the analytical solution of the E_f which can expand as the following form:

$$\sum_{q=1}^{N}((k_1\Delta\varphi_1 - \boldsymbol{J}_1^T\boldsymbol{w})^2 + ... + (k_n\Delta\varphi_n - \boldsymbol{J}_n^T\boldsymbol{w})^2)_q \tag{2.12}$$

where $\boldsymbol{J}_i^T$ is the ith row of the $\boldsymbol{J}^T$. As it is clear from the equation all the k_i are decoupled and $E_f = \sum_{i=1}^{n} E_{f_i}$, in which E_{f_i} is:

$$E_{f_i} = \sum_{i=1}^{N}(k_i\Delta\varphi_i - \boldsymbol{J}_i^T\boldsymbol{w})_q^2 \tag{2.13}$$

Considering the above equations, the minimum value of E_f can be found using:

$$\frac{\partial E_f}{\partial \boldsymbol{k}} = [\frac{\partial E_{f_1}}{\partial k_1}, ..., \frac{\partial E_{f_n}}{\partial k_n}]^T = 0 \tag{2.14}$$

Thus the optimal value of k_i will be as follows:

$$k_i = \frac{\sum_{p=1}^{N}(\boldsymbol{J}_i^T\boldsymbol{w}\Delta\varphi_i)_p}{\sum_{p=1}^{N}(\Delta{\varphi_i}^2)_p} \tag{2.15}$$

As mentioned earlier for finding the minimum value of E_f, the minimum value of each E_{f_i} should be found. Expanding E_{f_i} results into a quadratic function of k_i as follows:

$$k_i^2\sum_{q=1}^{N}(\Delta\varphi_i)_q^2 - 2k_j\sum_{q=1}^{N}(\boldsymbol{J}_i^T\boldsymbol{w}\Delta\varphi_i)_q + \sum_{q=1}^{N}(\boldsymbol{J}_i^T\boldsymbol{w})_q^2 \tag{2.16}$$

As we discuss through the following examples, since there is no limit on the DoF in our proposed methodology, it is more convenient to consider equal length for the segments and increase the precision of the PRB model by increasing DoF. There are also other advantages of the PRB model with equal lengths of the segments, which will be discussed in the examples. For the equal length of

the segment Eq. (2.15) explicitly gives the optimal stiffness values for the PRB model. Thus, the PRB model optimization simplifies to a great extent, offering higher precision, and can work for the various case of HFMs problems. The proposed method is summarized as Algorithm 2. In the next section, we show the application of the proposed method for different case studies in surgical robotics.

Algorithm 2 Proposed method for the PRB modeling of HFMs

initialize $S > 0$, $EI(s)$, $r(s)$ and $N, n \in \mathbb{N}$
Require: $\boldsymbol{w}_q$ for $q \in \mathbb{N}$ ▷ w_qs should cover the actual loading conditions of the HFM
$l_i = l$ and $l = \frac{S}{n}$
$\hat{x}_i^0$ & $\hat{y}_i^0$ for $i = 1 : n \leftarrow$ solve (2.3) for $w = [0, 0, 0]^T$
$\hat{\theta}_i^0$ for $i \in \{1 : n\} \leftarrow$ solve (2.11)
for $q = 1 : N$ **do**
    $\hat{x}_i$ & $\hat{y}_i$ for $i \in \{1 : n\} \leftarrow$ solve (2.3) for $\boldsymbol{w}_q$ over $n + 1$ equidistance points as $[0, l, ..., nl]$
    $\hat{\theta}_i^q$ for $i \in \{1 : n\} \leftarrow$ solve (2.11)
    $\delta\varphi_i^q = \hat{\theta}_i^q - \hat{\theta}_i^0$ for $i \in \{1 : n\}$
    $J^q \leftarrow$ solve (2.8)
end for
k_i for $i \in \{1 : n\} \leftarrow$ solve (2.15)

2.4 Versatility of the Proposed PRB Modeling Framework

We consider five practical case studies to investigate the versatility of the proposed strategy for PRB modeling. In the first case, we use the proposed method for modeling the catheter/guide wire. A catheter is a thin wire inserted into the blood vessel for endovascular interventions, such as stenosis treatment. As illustrated in Fig. 2.5, the catheter interacts with the blood vessels through the contact point with the arterial wall. Such interaction with the vessel might result in large contact forces, damaging the vessels. Determining catheter interaction contact forces can improve the safety and efficiency of navigation processes, preventing injuries in both manual and robotic vascular interventions [88]. The force interaction of the catheter with the arterial wall can be estimated using an image-based algorithm combined with a force/deformation model of the catheter [89]. The proposed PRB formulation can be used for the force/deformation model of the catheter in contact with the arterial wall. Note that this application requires knowledge of the last contact point before the tip end of the catheter. Another application of the proposed method is to model the force/deflection of the catheter with the arteries in 2D, which requires the exact location of the

contact points. As reported in [89], catheter has a variable stiffness along the length. We use our method to analyze such a problem in a separate case study.

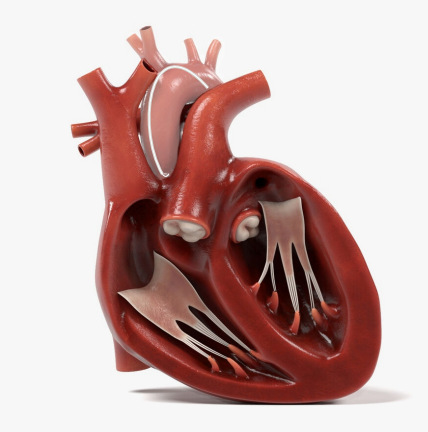

Figure 2.5: A catheter inside the aorta interacting with the arterial wall

In another scenario, we use the proposed method to model CTRs. The CTRs are comprised of super-elastic initially-curved tubes fitted inside each other in a telescopic way. The relative motion of the tubes (i.e., rotation and insertion) can be used to control the CTR shape and the position of its tip. CTRs are considered the smallest CR; hence they are a unique candidate for miniaturized surgeries such as retinal surgeries. CTRs in vitreoretinal surgery provide dexterity enhancement for controlling the tip angle of the instrument with respect to the retina (see Fig. 2.6). Additionally, they do not have the complication of the rigid robot, which imposes an extra force on the entry port at the sclera surface. Each CTR section can be considered an HFM with a constant predefined initial curvature. CTRs generally are made of constant curvature segments due to the complexity of the initially-curved elements in both modeling and manufacturing. In what follows, we use the proposed method to obtain a PRB model for both constant curvatures HFM and initially-curved ones for 2D CTRs. The PRB model can be used for indirect force estimation of the CTR only by knowing the tip deflection.

Considering the above-mentioned case studies, in the remainder of this section, we provide the optimal stiffness values for equal length PRB estimation over various ranges of DoF. However, we also consider the 3-DoF PRB models with non-identical segment lengths for the first case study. In each case study, apart from the optimal parameters, the precision of the method is also analyzed

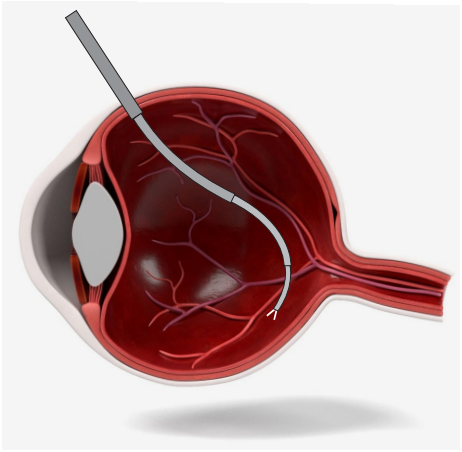

Figure 2.6: CTR for vitreoretinal surgeries, dexterity enhancement and reducing interaction force with the sclera at the entry port

by providing both position and force estimation errors. The errors are all normalized MAE in percentage, as follows:

$$\begin{cases} e_x = \frac{1}{N}\sum_{q=1}^{N}|\frac{x_t-\hat{x}_n}{S}|^q \times 100 \\ e_y = \frac{1}{N}\sum_{q=1}^{N}|\frac{y_t-\hat{y}_n}{S}|^q \times 100 \\ e_\theta = \frac{1}{N}\sum_{q=1}^{N}|\frac{\theta_t-\hat{\theta}_{n+1}}{\theta_t^0}|^q \times 100 \\ e_{f_x} = \frac{1}{N}\sum_{q=1}^{N}|\frac{f_x-\hat{f}_x}{max(f_x)}|^q \times 100 \\ e_{f_y} = \frac{1}{N}\sum_{q=1}^{N}|\frac{f_y-\hat{f}_y}{max(f_y)}|^q \times 100 \\ e_m = \frac{1}{N}\sum_{q=1}^{N}|\frac{m_t-\hat{m}_t}{max(m_t)}|^q \times 100 \end{cases} \tag{2.17}$$

in which $[\hat{f}_x, \hat{f}_y, \hat{m}_t]^T = \boldsymbol{J}^{-T}\boldsymbol{K}\boldsymbol{\Delta\varphi}$.

2.4.1 PRB Modeling of Straight HFMs

For the modeling of the catheter with the proposed approach, we consider a catheter with the parameters and loading conditions as described in [58]. The maximum length of the catheter is chosen to be 50 mm with an elastic modulus E of 350 MPa and an area moment of inertia $I = 4.91 \times 10^{-2}$ mm^4. The maximum and minimum values of the tip force are 4 mN and -4 mN, respectively, and the range of the tip moment is $[-250, 250]$ mN.mm. The analysis is done for 3410 loading combinations within the above range. First, we investigate the performance of the proposed

method for different segment lengths. This analysis is carried out for 82 combinations of segments l_i such that $l_1 + l_2 + l_3 = S$, as shown in Fig. 2.7.

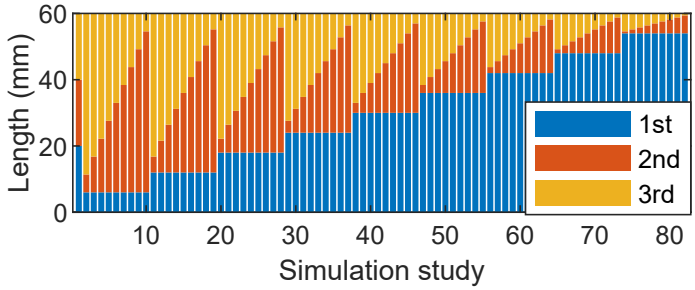

Figure 2.7: Various combinations of segment lengths for the 3-DoF PRB model

For these simulations, the stiffness of each joint is summarized in Fig. 2.8. It can be observed from this figure that the stiffness of the joints decreases by increasing the length of the corresponding segment, as expected physically. As for the HFM with uniform flexural rigidity along the length, the smaller the length of the segments, the larger the corresponding stiffness of the PRB model.

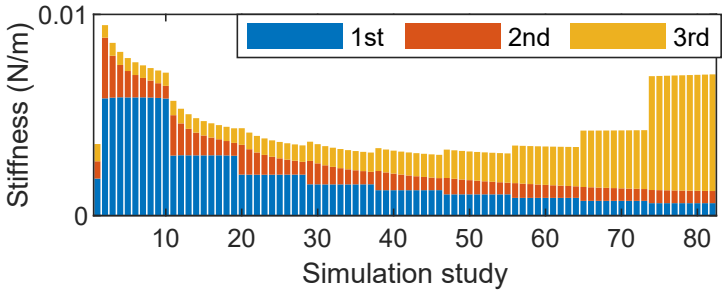

Figure 2.8: Stiffness values for the 3-DoF PRB models with various combinations of the segment lengths

The MAE of the position of the PRB models for all the 82 configurations is summarized in Fig. 2.9. It is to be noted that for all the case studies, both the position and force errors are normalized and represented in percentage. As observed, the minimum MAE for the tip angle occurs when the length of the third segment is smaller, which is expected from the mechanical characteristics of the system. Distinguishing the position error as e_x, e_y, and e_θ provides an informed opportunity to choose the right PRB model for each application. The normalized force/moment percentage errors for all the combinations of the segment length are also depicted in Fig. 2.10.

Considering equal length for the segments, we have developed five different PRB models for

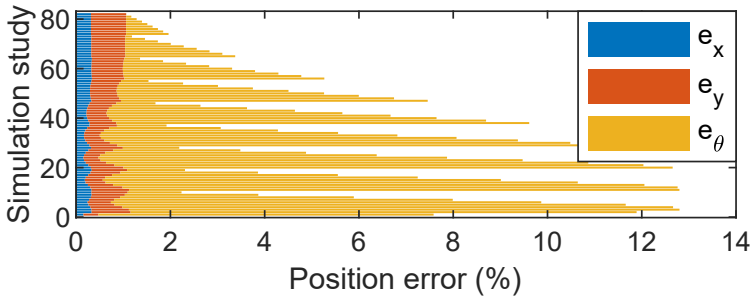

Figure 2.9: Position errors for the 3-DoF PRB models with various combinations of the segment lengths

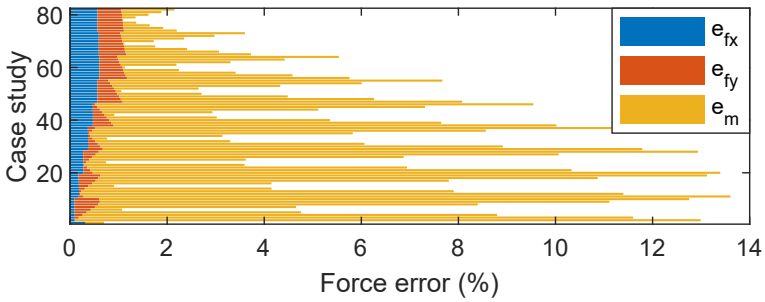

Figure 2.10: Force errors for the 3-DoF PRB models with various combinations of the segment lengths

the straight catheter. Each PRB model has a different DoF, and accordingly, the lengths of the segments are also different. The corresponding stiffness values for these PRB models are provided in Table 2.2. From these stiffness values, one can conclude that for each PRB model, there are only two values for the stiffness of the joints. The first value is for the stiffness of the first joint, and the second value is for that of the remaining joints (which have equal stiffness). It is to be noted that this result is only applied to the equal-length PRB models using the proposed methodology. This simplifies the analysis of the PRB model, especially when dealing with variable-length HFMs.

The force and position percentage error of each PRB model discussed above is also given in Table 2.3. These error values show that by increasing the DoF, all errors decrease. Therefore, one can choose the PRB model which best suits the specific application by adjusting the DoF properly.

Table 2.2: Optimal stiffness values for several PRB models of catheter

DoF	3	4	10	15	20
k_1	0.0019	0.0024	0.0059	0.0087	0.0116
k_2	0.0009	0.0011	0.0029	0.0043	0.0057
k_3	0.0009	0.0011	0.0029	0.0043	0.0057
k_4	N/A	0.0011	0.0029	0.0043	0.0057
k_{5-10}	N/A	N/A	0.0029	0.0043	0.0057
k_{15-20}	N/A	N/A	N/A	0.0043	0.0057

Table 2.3: Position and force errors of the catheter PRB models

DoF	3	4	10	15	20
e_{px}	0.2081	0.1242	0.0189	0.0079	0.0041
e_{py}	0.2956	0.1834	0.0266	0.0112	0.0058
$e_{p\psi}$	6.9509	5.3135	1.8691	1.08647	0.6990
e_{fx}	0.2683	0.2006	0.0772	0.0512	0.0382
e_{fy}	0.0168	0.0129	0.0018	0.0008	0.0005
e_m	0.3738	0.2515	0.0410	0.0188	0.0106

2.4.2 PRB Modeling of Constant-curvature HFMs

In this subsection, we consider a case study using CTRs. An example of a miniaturized CTR is presented in [25], which is primarily developed for vitreoretinal surgeries. This CTR is comprised of two sections with the parameters specified in Table 2.4. Considering nitinol as the material, the elastic modulus of the tubes is 71 GPa.

Table 2.4: Parameters of a CTR designed for eye surgery

Tube type	Inner tube	Outer tube
Inner diameter (mm)	0.203	0.432
Outer diameter (mm)	0.406	0.635
Radius of curvature (mm)	27	80
Total length (mm)	27	26.5

For the case of membrane peeling, which is a retinal surgery, the range of forces is less than 7.5 mN [34]. Considering the force limit and the maximum length of 27 mm for the curved element, the maximum torque for the PRB model is assumed to be 200 mN.mm. The PRB model is to be optimized for the inner tube for 6820 loading cases over the range of loads $f \in [0, 7.5]$ mN, $\psi \in [0, 2\pi]$ and $m_t \in [0, 200]$ mN.mm.

Table 2.5: Optimal stiffness values of the CTR PRB models

DoF	3	4	10	15	20
k_1	0.0205	0.0271	0.0666	0.0995	0.1323
k_2	0.0099	0.0132	0.0329	0.0493	0.0658
k_3	0.0099	0.0132	0.0329	0.0493	0.0658
k_4	N/A	0.0132	0.0329	0.0493	0.0658
k_{5-10}	N/A	N/A	0.0329	0.0493	0.0658
k_{11-15}	N/A	N/A	N/A	0.0493	0.0658
k_{16-20}	N/A	N/A	N/A	N/A	0.0658

As it can be observed from the results in Table 2.5, for this case study, like the first one, which used the catheter PRB model, there are only two values for the stiffness of the joints, regardless of the DoF. In Table 2.6 the values of the tip position error and force estimation error are for this PRB model.

Table 2.6: Position and force errors of CTR PRB models

DoF	3	4	10	15	20
e_{px}	0.3897	0.2183	0.0337	0.0142	0.0074
e_{py}	0.2137	0.1197	0.0185	0.0078	0.0040
$e_{p\theta}$	0.5353	0.3919	0.1357	0.0791	0.0508
e_{fx}	0.1373	0.1019	0.0400	0.0265	0.0199
e_{fy}	0.0168	0.0096	0.0016	0.0007	0.0004
e_m	0.5948	0.3428	0.0569	0.0255	0.0144

The results show that by increasing the DoF of the PRB model, the overall error for both position and force decreases.

2.4.3 PRB Modeling of Initially-curved HFM with a variable curvature

As discussed in Section 2.2, one of the limitations of the available PRB modeling methods is in the modeling of HFMs, where the curvature changes along the length. To the best of the authors' knowledge, there is no PRB research that can directly obtain a PRB model for HFM with variable curvature along the length. On the other hand, for the HFM with a circular shape, while it is theoretically assumed that the curvature is constant along the length, irregularities in the shape are inevitable during the manufacturing process. Additionally, the mechanical elements will have plastic deformation over time which appears as a shape change. With an initially-curved HFM, there

is more flexibility in the optimal design of HFM-based systems, such as constant force grippers. However, the limitations of the conventional methods complicate the possibility of the parametric design of nonuniform curvature HFMs. In the sequel, we investigate the performance of the proposed PRB modeling approach for the HFMs with a variable curvature along the length in the no-load condition. For example, we consider the curvature to be linearly varying along the length, i.e., $r(s) = a \cdot s + b$, where a and b are known constants. Let the curvature be 27 mm at the base and 9 mm at the tip point. The loading condition and other parameters are like the previously presented constant curvature case study for the CTR. The optimal values of the stiffness of the PRB model are given in Table 2.7, which shows that except for the 3-DoF model, all other ones have two values for the stiffness of the PRB model. In Table 2.8, the values of the tip position error and force estimation error have been represented for the PRB model.

Table 2.7: Optimal stiffness values for PRB models of an initially-curved HFM with variable initial curvature

DoF	3	4	10	15	20
k_1	0.0205	0.0270	0.0665	0.0993	0.1319
k_2	0.0099	0.0132	0.0329	0.0493	0.0658
k_3	0.0130	0.0132	0.0329	0.0493	0.0658
k_4	N/A	0.0132	0.0329	0.0493	0.0658
k_{5-10}	N/A	N/A	0.0329	0.0493	0.0658
k_{11-15}	N/A	N/A	N/A	0.0493	0.0658
k_{16-20}	N/A	N/A	N/A	N/A	0.0658

Table 2.8: Position and force errors for PRB models of an initially-curved HFM with variable initial curvature

DoF	3	4	10	15	20
e_{px}	5.9569	0.3590	0.0584	0.0247	0.0129
e_{py}	0.9082	1.1030	0.1697	0.0714	0.0371
$e_{p\theta}$	0.8184	0.3919	0.1357	0.0791	0.0508
e_{fx}	0.1868	0.1001	0.0403	0.0269	0.0202
e_{fy}	0.0420	0.0199	0.0030	0.0013	0.0007
e_m	2.0934	0.7897	0.1158	0.0505	0.0281

2.4.4 PRB Modeling of Straight HFMs with Nonuniform Stiffness

The flexural stiffness is represented by the product of E and I. Thus, if the cross-section of the HFMs is nonuniform or the material properties are not uniform along the length, the flexural stiffness would be variable. This is the case for the catheter, where the flexural stiffness decreases from the base to the tip point. As a case study, we consider the catheter described in 2.4.1 under a similar loading condition and let the stiffness be variable along the length. For this analysis, the distribution of the stiffness is assumed to be linearly varying along the length, expressed as $EI(s) = -\frac{E \cdot I}{2S} s + E \cdot I$.

The results of the PRB model for various DoF is presented in Table 2.9. As expected, we have different values for the joint stiffness in each PRB model. The error of PRB approximation for this case study is provided in Table 2.10.

Table 2.9: Optimal stiffness values of the PRB models for a HFM with non-uniform stiffness

DoF	3	4	10	15	20
k_1	0.0063	0.0086	0.0224	0.0339	0.0454
k_2	0.0028	0.0040	0.0109	0.0166	0.0224
k_3	0.0022	0.0034	0.0103	0.0160	0.0218
k_4	N/A	0.0028	0.0097	0.0155	0.0212
k_5	N/A	N/A	0.0092	0.0149	0.0206
k_6	N/A	N/A	0.0086	0.0143	0.0201
k_7	N/A	N/A	0.0080	0.0137	0.0195
k_8	N/A	N/A	0.0074	0.0132	0.0189
k_9	N/A	N/A	0.0069	0.0126	0.0183
k_{10}	N/A	N/A	0.0063	0.0120	0.0178
k_{11}	N/A	N/A	N/A	0.0114	0.0172
k_{12}	N/A	N/A	N/A	0.0109	0.0166
k_{13}	N/A	N/A	N/A	0.0103	0.0160
k_{14}	N/A	N/A	N/A	0.0097	0.0155
k_{15}	N/A	N/A	N/A	0.0092	0.0149
k_{16}	N/A	N/A	N/A	N/A	0.0143
k_{17}	N/A	N/A	N/A	N/A	0.0137
k_{18}	N/A	N/A	N/A	N/A	0.0132
k_{19}	N/A	N/A	N/A	N/A	0.0126
k_{20}	N/A	N/A	N/A	N/A	0.0120

Table 2.10: Position and force errors for the PRB models of a HFM with non-uniform stiffness

DoF	3	4	10	15	20
e_{px}	0.0051	0.0028	0.0004	0.0002	0.0001
e_{py}	0.1112	0.0633	0.0099	0.0042	0.0022
$e_{p\theta}$	3.1931	2.4242	0.8994	0.5328	0.3452
e_{fx}	0.0827	0.0635	0.0317	0.0261	0.0238
e_{fy}	0.0144	0.0139	0.0169	0.0178	0.0183
e_m	0.3195	0.2203	0.3410	0.3847	0.4071

2.4.5 PRB Modeling of the initially-curved Variable-length HFMs

In CTRs, the initially curved segments are telescopically constrained, and the relative position of the segments allows the tip of the robot to follow a specified trajectory. Thus, a suitable model of the robot should consider the variable length of each curved segment. From the results obtained in the previous case studies, the PRB model for the equal length of the segments is specified with three parameters. These three parameters are k_1, which is the stiffness of the first joint, k_2, which is the stiffness of the other joints, and the length of each segment (i.e., S/n). Considering this fact, k_1 and k_2 can be found as functions of the total length of the curved segment while keeping the DoF of the PRB model the same. In other words, for a HFM with the length of $S = L$ first we develop an n-Dof PRB model with k_1, k_2 and $l = L/n$ as the PRB model parameters, then we develop another n-DoF PRB model for the same HFM which has a different length , i.e. $S = L + \Delta L$, with $k_1{}'$, $k_2{}'$ and $l' = (L + \Delta L)/n$ being the parameters of the PRB model. By repeating this procedure for several ΔL, one can find a function that gives k_1 and k_2 as a function of HFM length. Fig. 2.11 shows the stiffness values of a 30-DoF PRB model as a function of the HFM length. This study shows that the stiffness values of the PRB model for variable-length HFM (i.e., k_1 and k_2), with the proposed approach, can be represented with a power function, represented as follows:

$$k = \kappa s^{-\sigma} \tag{2.18}$$

where κ and σ are the tuning parameters.

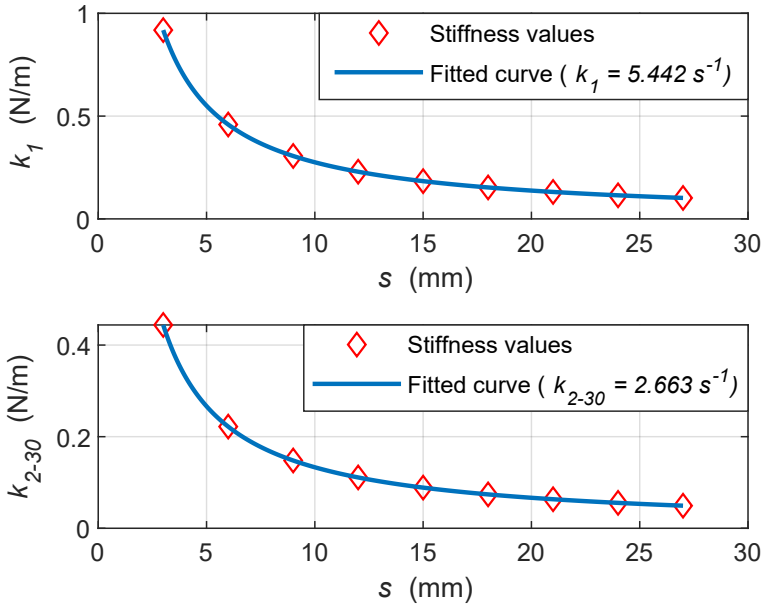

Figure 2.11: Optimal stiffness for the 30-DoF PRB model of a variable-length HFM as a function of HFM length

Chapter 3

Stiffness Modeling

3.1 Background

The stiffness of a robot is defined as the resistance to deformation under external force or torque applied to its end-effector [52], or the tip of the robot in a continuum robot (CR). Stiffness is one of the critical parameters in analyzing a robot interacting with the environment. A sufficiently accurate value of this parameter is essential for both the position and force control of the robotic systems. The stiffness can be mathematically expressed in a matrix form. Two different matrix representations for stiffness are introduced in the literature: Cartesian stiffness matrix and joint-space stiffness matrix. The joint-space stiffness matrix describes the deflection of the robot joints to the corresponding static forces/torque by considering virtual springs to model the deformation at the joints. On the other hand, the Cartesian stiffness matrix describes the relationship between the deformation of the robot tip or end-effector under the applied force/torque at the tip. Thus, by accurately knowing the Cartesian stiffness, one can indirectly measure the applied force at the robot tip by only measuring its deflection. Additionally, in the position control problem, the resultant error highly depends on the Cartesian stiffness of the robot. Hence, Cartesian stiffness plays a key role in the force control schemes. On the other hand, joint space stiffness depends only on the stiffness of the joints, as a constant characteristic of the robot, unlike the Cartesian stiffness that is configuration-dependent and depends on the external load or the deformation of the robot. The formulation of the Cartesian stiffness is a complex problem even for robots with rigid linkages [52].

There are three main methods for modeling the Cartesian stiffness of highly flexible members (HFM): virtual joint method, finite element method, and matrix structural method [52]. Due to the computational cost of the matrix structural and finite element methods, these methods are not suitable for real-time applications [53]. In the virtual joint method, the joint space stiffness is utilized to formulate the Cartesian stiffness using the Jacobian of the robot. Each stiffness matrix can be converted to the other using the Conservative Congruency Transformation [90]. There are two methods for formulating Cartesian stiffness via the virtual joint method, namely, the constant stiffness method and the enhanced stiffness method, developed for rigid robots. To the best of our knowledge, there is no literature on the Cartesian stiffness modeling of CRs, since the Cartesian stiffness is configuration-dependant, and the proposed methods cannot capture large deformation of HFMs. Studies use the constant stiffness model [86]. This chapter shows that the existing Cartesian stiffness models fail to describe the force/deflection behavior of HFMs adequately.

To address the limitations of the existing methods, we propose a novel methodology for the Cartesian stiffness of HFMs using the virtual joint method. As mentioned earlier, the virtual joint method requires joint space stiffness, for which we use the pseudo-rigid body (PRB) modeling method proposed in the previous chapter to find the corresponding matrix. Note that finding an accurate joint stiffness is one of the challenges in the virtual joint method [53]. Thanks to the proposed PRB method, we have a high-precision joint stiffness model for Cartesian stiffness formulation.

3.2 Existing Models for Cartesian Stiffness

The earliest Cartesian stiffness model for the robotic systems was introduced by Salisbury [38] for the serial robotic arms in 1980, which we refer to as the conventional method defined as Eq. (3.1).

$$\boldsymbol{K} = (\boldsymbol{J}^T)^\dagger \boldsymbol{K}_\varphi \boldsymbol{J}^\dagger \tag{3.1}$$

where $\boldsymbol{K}$ is the Cartesian stiffness, $\boldsymbol{K}_\varphi$ is the joint space stiffness of the robot, and $\dagger$ represents the pseudo-inverse for non-square matrices. Eq. (3.1) is the stiffness model commonly used in the literature, which relates the stiffness to the configuration of the robot and the joint stiffness matrix. In [90], Chen and Kao added remarks on the Salisbury model, discussing that it is only valid in

the equilibrium configuration of the robots without external load. It is also shown in [90] that the stiffness matrix is symmetric. Differentiating the static force mapping relation $\boldsymbol{\tau} = \boldsymbol{J}^T \boldsymbol{w}$ results in:

$$\frac{\partial \boldsymbol{\tau}}{\partial \boldsymbol{\varphi}} = \frac{\partial \boldsymbol{J}^T}{\partial \boldsymbol{\varphi}} \boldsymbol{w} + \boldsymbol{J}^T \frac{\partial w}{\partial \boldsymbol{\varphi}} \tag{3.2}$$

Substituting $\frac{\partial \boldsymbol{w}}{\partial \varphi}$ with $\frac{\partial \boldsymbol{w}}{\partial \boldsymbol{p}} \frac{\partial \boldsymbol{p}}{\partial \boldsymbol{\varphi}}$ and using the definition of the Jacobian as $\boldsymbol{J} = \frac{\partial \boldsymbol{p}}{\partial \boldsymbol{\varphi}}$ yields:

$$\boldsymbol{K}_\varphi = \frac{\partial \boldsymbol{J}^T}{\partial \boldsymbol{\varphi}} \boldsymbol{w} + \boldsymbol{J}^T \frac{\partial \boldsymbol{w}}{\partial \boldsymbol{p}} \boldsymbol{J} \tag{3.3}$$

On the other hand by definition, $\frac{\partial \boldsymbol{w}}{\partial \boldsymbol{p}} = \boldsymbol{K}$. Thus, the Cartesian stiffness of the robot is given by [90]:

$$\boldsymbol{K} = (\boldsymbol{J}^T)^\dagger (\boldsymbol{K}_\varphi - \frac{\partial \boldsymbol{J}^T}{\partial \varphi} \boldsymbol{w}) \boldsymbol{J}^\dagger \tag{3.4}$$

The Cartesian stiffness in the above equation consists of two terms. The first term is $(\boldsymbol{J}^T)^\dagger \boldsymbol{K}_{\boldsymbol{\varphi}} \boldsymbol{J}^\dagger$, which is the elastic stiffness and the second term is $-(\boldsymbol{J}^T)^\dagger (\frac{\partial \boldsymbol{J}^T}{\partial \boldsymbol{\varphi}} \boldsymbol{w}) \boldsymbol{J}^\dagger$, which represents the change of configuration due to the applied load. The term $\frac{\partial \boldsymbol{J}^T}{\partial \boldsymbol{\varphi}} \boldsymbol{w}$ is denoted by $\boldsymbol{K}_g$, referred to as *geometrical stiffness*, and can be written in the following matrix form:

$$\boldsymbol{K}_g = \begin{bmatrix} \frac{\partial \boldsymbol{J}^T}{\partial \varphi_1} \boldsymbol{w} & \dots & \frac{\partial \boldsymbol{J}^T}{\partial \varphi_n} \boldsymbol{w} \end{bmatrix} \tag{3.5}$$

Remark 3.1 It follows from Eq. (3.2) that when there is no external force ($\boldsymbol{w} = 0$) or when the Jacobian of the robot is constant (i.e., in the case of isotropic mechanism), the stiffness equation is simplified as Eq. (3.1).

Remark 3.2 Obtaining $\boldsymbol{K}_g$ requires the knowledge of the external force at the tip $\boldsymbol{w}$, which limits its application in practice. It is due to the fact that there are applications where direct measurement of the force is not feasible (e.g., using concentric tube robots for vitreoretinal surgeries).

3.3 A Novel Approach for Modeling Stiffness in HFMs

Replacing the HFM with an equivalent PRB model, we start by finding the deflection of the virtual joints of the PRB model for a given deflection at the tip of the robot. In other words, we

estimate the inverse kinematic (IK) and use the deformation of the PRB model virtual joints to find the Cartesian stiffness. This is done by minimizing the potential energy of the deformed PRB model and via introducing a new expression for the Jacobian of the deformed HFM as follows:

$$\boldsymbol{J}_d = \boldsymbol{J}_0 + \eta \frac{\partial \boldsymbol{J}}{\partial \boldsymbol{\varphi}} \boldsymbol{\Delta\varphi}_0 \tag{3.6}$$

where $\boldsymbol{J}_0$ is the no-load Jacobian, $\boldsymbol{\Delta\varphi}_0 = J_0^{-1}\Delta\hat{p}$, and η is a tuning parameter which is considered to be 0.5 for simplification. The selection of suitable value for η is elaborated in various studies (e.g., see [91, 92]). Additionally, $\boldsymbol{J}_d$ is the deformed Jacobian and $\frac{\partial \boldsymbol{J}}{\partial \boldsymbol{\varphi}}\Delta\boldsymbol{\varphi}_0$ is found as follows:

$$\frac{\partial \boldsymbol{J}}{\partial \boldsymbol{\varphi}}\Delta\boldsymbol{\varphi}_0 = \begin{bmatrix} \frac{\partial \boldsymbol{J}}{\partial \varphi_1}\Delta\boldsymbol{\varphi}_0 & \dots & \frac{\partial \boldsymbol{J}}{\partial \varphi_n}\Delta\boldsymbol{\varphi}_0 \end{bmatrix} \tag{3.7}$$

By using the proposed Jacobian for the deformed HFM, one can write $\boldsymbol{J}_d\Delta\boldsymbol{\varphi} = \Delta\hat{p}$. Thus, for finding $\Delta\boldsymbol{\varphi}$, the inverse of the Jacobian is required. For the case of an n-degrees-of-freedom (DOF) PRB model, the Jacobian is non-square; hence, there are infinitely many solutions for the inverse of the Jacobian. By considering the energy minimization as a cost function, we define an optimization problem formulated as:

$$\begin{cases} E_k = \frac{1}{2}\Delta\boldsymbol{\varphi}^T \boldsymbol{K}_\varphi \Delta\boldsymbol{\varphi} \\ \text{subject to: } \boldsymbol{J}_d\Delta\boldsymbol{\varphi} = \Delta\boldsymbol{p} \end{cases} \tag{3.8}$$

where E_k is the stored potential energy in the virtual springs of the PRB model. This constrained optimization problem can be solved using Lagrange multipliers [93], i.e.:

$$L(\Delta\boldsymbol{\varphi}, \boldsymbol{\lambda}) = \frac{1}{2}\Delta\boldsymbol{\varphi}^T \boldsymbol{K}_\varphi \Delta\boldsymbol{\varphi} + \boldsymbol{\lambda}^T(\boldsymbol{J}_d\Delta\boldsymbol{\varphi} - \Delta\boldsymbol{p}) \tag{3.9}$$

where λ is the Lagrange multipliers vector. The minimal value of L in Eq. (3.9) can be found by setting its derivatives with respect to $\boldsymbol{\lambda}$ and $\Delta\boldsymbol{\varphi}$ to zero as follows:

$$\begin{cases} \frac{\partial L}{\partial \Delta\boldsymbol{\varphi}} = 0 \\ \frac{\partial L}{\partial \boldsymbol{\lambda}} = 0 \end{cases} \rightarrow \begin{bmatrix} \Delta\boldsymbol{\varphi} \\ \boldsymbol{\lambda} \end{bmatrix} = \begin{bmatrix} K_\varphi & \boldsymbol{J}_d{}^T \\ \boldsymbol{J}_d & 0 \end{bmatrix}^{-1} \begin{bmatrix} 0 \\ \Delta\boldsymbol{p} \end{bmatrix} \tag{3.10}$$

Using the inverse of the $2\times$ 2 block matrices [94], one can solve the above equation, such that:

$$\Delta\boldsymbol{\varphi} = \boldsymbol{K}_{\varphi}^{-1}\boldsymbol{J}_d^T(\boldsymbol{J}_d\boldsymbol{K}_{\varphi}^{-1}\boldsymbol{J}_d^T)^{-1}\Delta\boldsymbol{p} \tag{3.11}$$

where $\boldsymbol{K}_{\varphi}^{-1}\boldsymbol{J}_d^T(\boldsymbol{J}_d\boldsymbol{K}_{\theta}^{-1}\boldsymbol{J}_d^T)^{-1}$ is the weighted pseudo-inverse of $\boldsymbol{J}_d$, and $\boldsymbol{\Delta}\varphi$ lies within the null space of $\boldsymbol{J}_d$. On the other hand, from the force mapping formula $\boldsymbol{w} = (\boldsymbol{J}_0^T)^{\dagger}\boldsymbol{\tau}$ and definition of the joint space stiffness $\boldsymbol{\tau} = \boldsymbol{K}_{\varphi}\Delta\boldsymbol{\varphi}$:

$$\boldsymbol{w} = (\boldsymbol{J}_0^T)^{\dagger}\boldsymbol{K}_{\varphi}\Delta\boldsymbol{\varphi} \tag{3.12}$$

where J_0 is the no-load Jacobian. Substituting Eq. (3.11) into (3.12) yields:

$$\boldsymbol{w} = ((\boldsymbol{J}_0^T)^{\dagger}\boldsymbol{K}_{\varphi})(\boldsymbol{K}_{\varphi}^{-1}\boldsymbol{J}_d^T(\boldsymbol{J}_d\boldsymbol{K}_{\varphi}^{-1}\boldsymbol{J}_d^T)^{-1})\Delta\boldsymbol{p} \tag{3.13}$$

which gives the applied force at the tip in terms of the tip deflection. On the other hand, since $\boldsymbol{w} = \boldsymbol{K}\Delta\boldsymbol{p}$, the Cartesian stiffness of the HFM can be obtained as:

$$K = \boldsymbol{J}_0^{T\dagger}(\boldsymbol{J}_d^T(\boldsymbol{J}_d\boldsymbol{K}_{\varphi}^{-1}\boldsymbol{J}_d^T)^{-1}) \tag{3.14}$$

Remark 3.3 Eq. (3.11) is a solution to the IK of the PRB model. As we showed in Chapter 2 the proposed PRB modeling method captures the deflection of the HFM and can adequately work as an alternative to the continuum model. As illustrated in Fig. 2.4 the shape of the PRB model under the tip load follows that of the continuum model. Thus, this equation can be used for the shape estimation of HFM under tip load.

In what follows; first we investigate the performance of the proposed stiffness model through simulation studies and compare it to the constant stiffness and enhanced stiffness models. Then, to evaluate the proposed IK model, we compare the deflection obtained from Eq. (3.11) with that of the PRB model for a 20-DoF PRB model of an initially curved HFM.

3.4 Validation Studies of the Proposed Stiffness Model

In this section, we compare the performance of the proposed method in estimating the force of the initially curved HFM under tip loading using the tip deflection and the Cartesian stiffness model. We compare the proposed results with that of the enhanced model (Eq. (3.4)) and the constant Cartesian stiffness model (Eq. (3.1)). Note that the enhanced stiffness model requires the knowledge of the force, making it infeasible in the application. However, the value of the force is available in simulation, and we investigate the validity of the method accordingly. For the comparison, we consider an initially-curved HFM as in Section 2.4.2 for which the optimal stiffness of the PRB model for various DoF was obtained. For a better visual comparison of the performance of the proposed method in an enlarged graph, we first consider three loads with magnitude $(0, 5, 10)$ mN applied at the tip with an angle over the interval $[0, 2\pi]$ with a step size of 0.1π leading to 120 loading cases. The comparison of the force estimation for these loading cases is illustrated in Figs. 3.1 and 3.2. Figs. 3.1 shows the performance of the proposed force estimation method compared to the constant stiffness and enhanced stiffness methods for a 4-DoF PRB model. These figures show that the proposed method outperforms the other two methods in terms of f_x and f_y estimation accuracy. However, the estimation of the proposed method still deviates from the actual force.

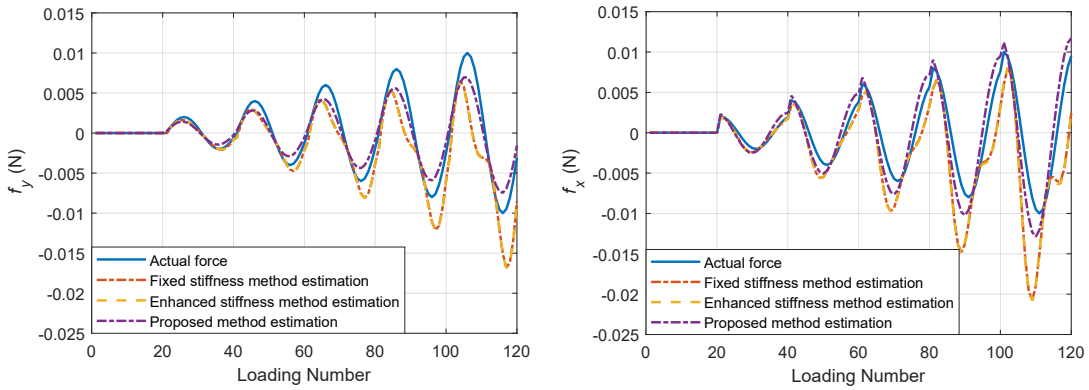

(a) (b)

Figure 3.1: Comparison of the force estimation of the proposed method for a 4-DoF PRB model with the constant stiffness and enhanced stiffness methods

In another study we use a 20-DoF PRB model, and the results of the force estimation are provided in Fig. 3.2. As shown in this figure, the performance of the constant stiffness and enhanced

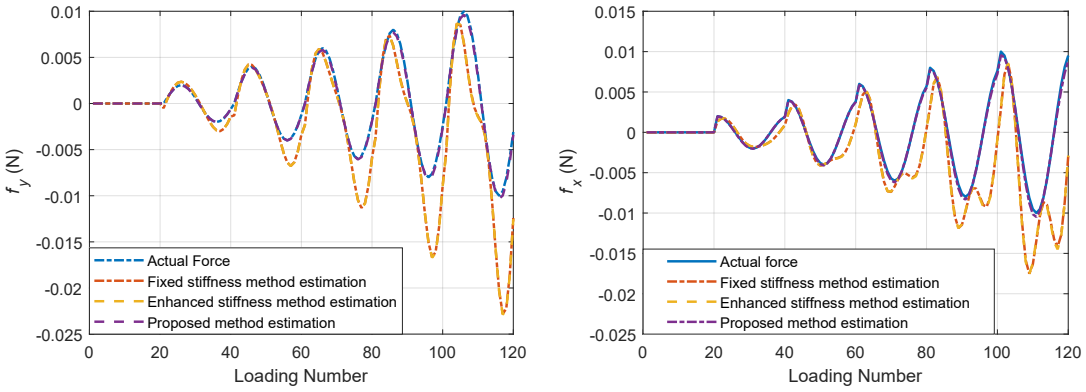

(a) (b)

Figure 3.2: Comparison of the force estimation of the proposed method for a 20-DoF PRB model with the constant stiffness and enhanced stiffness methods

stiffness formulation is close to each other, and their estimation error is relatively large. On the other hand, the proposed method can suitably estimate the force to a great extent. This study shows the importance of the proposed PRB model, which has no limit on the DoF, helping us have an accurate stiffness model. For a more precise comparison, we have increased the loading cases in the range of $[0, 10]$ mN with the step size of 0.1 mN in the same angle range as the previous study, which leads to 2020 loading cases. The absolute mean absolute error (MAE) of the force estimation of the proposed method can be compared to that of the constant stiffness and enhanced stiffness method in Fig. 3.3. As observed, the MAE of the force estimation in either directions is in the order of 10^{-4} N in the proposed method; however, for the other two methods, it is in the order of 10^{-2} N which shows the superior performance of the proposed method. The MAE for the three discussed methods is depicted in Table 3.1. As it is clear from the MAEs, the proposed method is almost 20 times more precise compared to both existing methods.

Table 3.1: MAE of the force estimation of different stiffness models

Errors	Constant Stiffness	Enhanced Stiffness	Proposed Method
MAE of $f_x(\%)$	25.414	25.649	1.277
MAE of $f_y(\%)$	19.001	19.175	0.873

In the above validation studies, we use $\eta = 0.5$. Now we evaluate the impact of η on the precision of the method for the above-discussed studies. Fig. 3.4 shows the MAE of the force

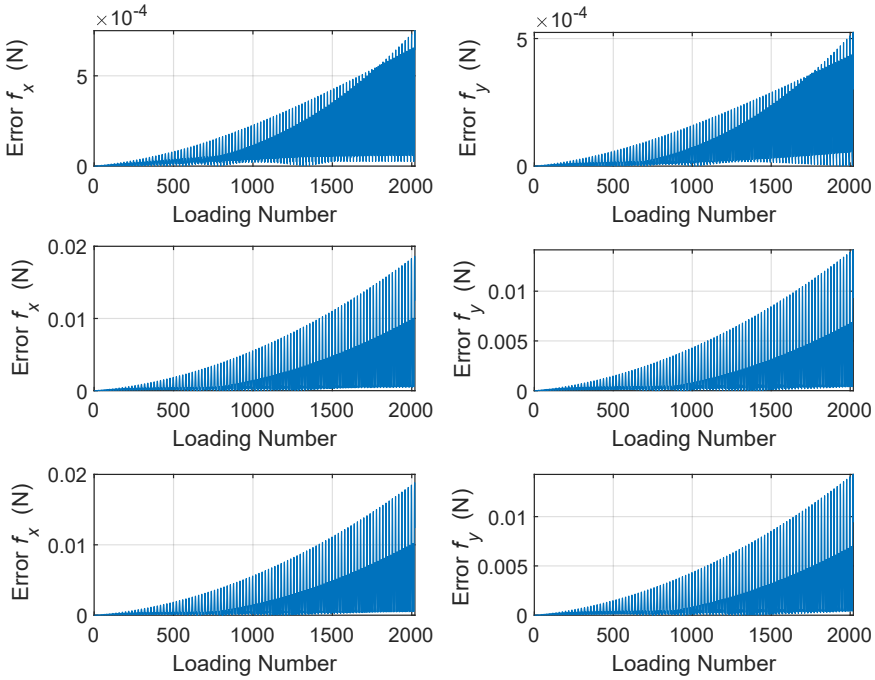

Figure 3.3: Comparison of the MAE of the force estimation of the proposed method (top figures), constant stiffness method (middle figures) and enhanced stiffness method (bottom figures)

estimation with respect to η.

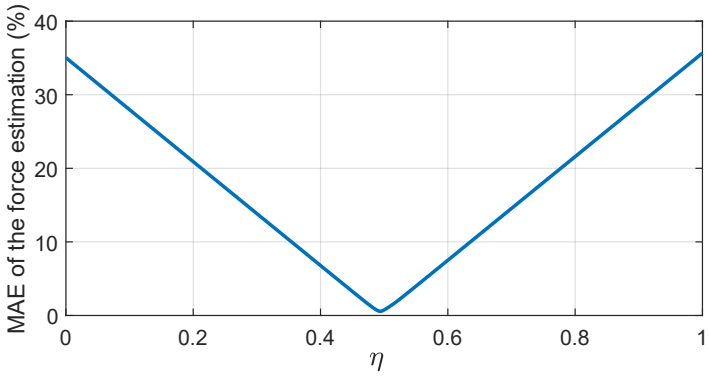

Figure 3.4: MAE of the force estimation for the proposed method with respect to η

As observed from the above figure, the smallest MAE occurs at $\eta = 0.4940$. The MAE for f_x and f_y estimations for this value of η are 0.2866% and 0.6197%, respectively.

3.5 Validation Studies of the Proposed IK Model

In this section, we investigate the performance of the proposed IK model (Eq. (3.11)) for estimating the deflection of HFM. Similar to the previous section, the 20-DoF PRB model of Section 2.4.2 is used as a reference. We compare the deflection of each joint of the PRB model and the proposed IK model for 120 loading cases. As observed from Fig. 3.5, the proposed IK model captures the deflection

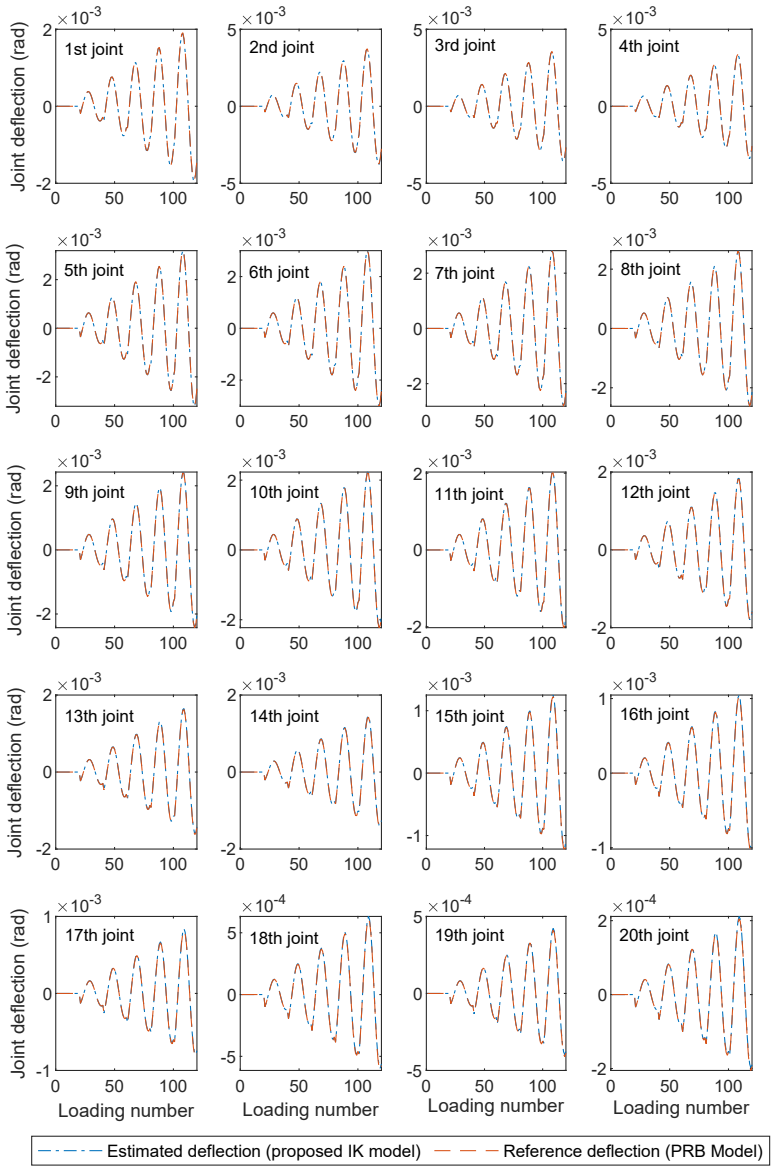

Figure 3.5: Joint deflections of the 20-DoF PRB model in 120 different loading conditions, compared to the estimated joint deflection via proposed IK model

Chapter 4

Indirect Hybrid Force/Position Control

4.1 Background

The compliant nature of the continuum robots (CR) allows them to penetrate deeper into the body cavities to perform the surgical intervention and provides added dexterity at the far end of the surgical instrument compared to conventional RMIS. These types of compliant systems, such as CRs, are limited in their accuracy and the value of the force they can apply. Additionally, compliance adds uncertainty and difficulties that degrades the trajectory tracking performance [95]. Thus, having a control method that can safely interact with the environment, maintain manipulation precision, and deliver adequate forces is a complex control challenge for CRs applications. Complications in vitreoretinal surgery are a result of excess and/or incorrect forces applied to ocular tissue [50]. To prevent damage to such tissues, as is the case in retinal membrane peeling, the surgeon requires to keep operative forces low and safe through delicate maneuvering. Membrane peeling is one of the common retinal surgeries in which a thin layer formed on the surface of the retinal (epiretinal membrane) is removed. Epiretinal membrane is about 5 μm thick, and high forces and velocities should be avoided during membrane peeling to prevent damage to the retinal. In general, during epiretinal membrane peeling the applied force should be under 7.5 mN [34] with the tip velocity of 100-500 μm/s [36]. Due to the high sensitivity of these procedures, 50% of the patients have injuries and defects after peeling [51]. Using robotic systems, the surgeon can benefit from higher precision in surgery. This section aims to design suitable controllers to satisfy the required

accuracy and the constraint of the retinal surgery using the concentric tub robot (CTR) as introduced in [96] for vitreoretinal surgeries. The proposed architecture is a hybrid robot consisting of an RCM mechanism to rotate the surgical instrument at the entry port and an initially curved flexible part with variable length. By changing the flexible segment length, the instrument's angle with respect to the surgical site and its compliance can be controlled.

4.1.1 Interaction Modeling of Initially-curved CRs

Consider a minimally invasive procedure, where the instrument is pivoted to the incision point O as depicted in Fig. 4.1. The setup comprises a rigid segment that can be rotated about the entry point and a flexible segment of length S. Such structure forms a CTR mounted on a rotating arm. This setup has two active degrees-of-freedom (DoF) for the rigid segment and one DoF for the flexible segment.

The control inputs to the robot for the rigid segment are denoted by q_1 and q_2, which are the length of the insertion and the rotation angle of the rigid segment. We also denote the control input for the length of the flexible segment with q_3. In Fig. 4.1, XY represents the fixed coordinate with the origin at the entry point, and xy is the relative coordinate system positioned at the distal end of the rigid segment. The compliant environment is modeled with a rigid flat surface connected to the base of stiffness k_e equivalent to the uni-directional stiffness of the soft tissue. The initial horizontal position of the environment is denoted by x_n in the xy plane, deflected by Δx_e when interacting with the robot. The interaction force of the robot with the environment is denoted by f_e. Note that epiretinal membrane surgery involves a vitrectomy and membrane peeling. During Vitrectomy, the jelly-like substance (vitreous humor) that generally fills the center of the eye is removed. Thus, from the entry point onward, the applied forces to the robot will be only the interaction force with the retina. Furthermore, as the surgical operation is a very slow process, the damping force, which is proportional to the velocity, can be neglected.

The deflection of the flexure segment under the applied load at the tip is a BVP that can be represented by an equation similar to Eq. (2.3) with one main difference. When the robot is in contact with a flexible surface, the value of f_e depends on the deflection of the soft environment and

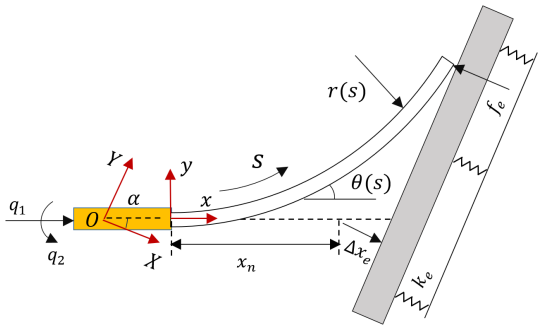

Figure 4.1: A hybrid robot with an initially-curved flexible tube, interacting with a soft environment

is proportional to it, such that:

$$f_e = -k_e \Delta x_e \tag{4.1}$$

where k_e is the stiffness of the environment. Based on the geometry of the problem, we can also write additional compatibility equations as follows:

$$\cot \alpha = \frac{y(S)}{x(S) - (x_n + \Delta x_e / \cos \alpha)} \tag{4.2}$$

where $(x(S), y(S))$ is the tip position of the robot. Rewriting the the above compatibility equations and putting them together with Eqs. (2.3) and (4.1), the governing equations of the interaction are represented as:

$$\begin{cases} \theta''(s) = \dfrac{m'(s)}{EI(s)} - \dfrac{EI'(s)m(s)}{EI^2(s)} - \dfrac{r'(s)}{r^2(s)} \\ x'(s) = cos\theta(s) \\ y'(s) = sin\theta(s) \\ \cot \alpha = \dfrac{y(S)}{x(S) - (x_n + f_e/(k_e \cos \alpha))} \\ \theta'(S) = \dfrac{m(S)}{EI(S)} + \dfrac{1}{r(S)} \\ \theta(0) = 0 \\ x(0) = 0 \\ y(0) = 0 \end{cases} \tag{4.3}$$

4.2 Existing Challenges for the Force Control of Concentric Tube Robots

The control variables in Eq. (4.3), are f_e, $x(S)$ and $y(S)$. However, controlling force and position in one single direction simultaneously cannot be performed independently, reducing the control variables to f_e and $y(S)$. On the other hand, the control inputs to the system are x_n and α. Note that x_n can be controlled via the insertion of the rigid segment q_1 or by changing the length of the flexible segment q_3. Controlling a system with boundary conditions is a complex problem, and the existing design methods are, in general, not suitable for real-time applications. On the other hand, for CRs, the static force mapping, requires the strain energy of the robot (i.e., ϵ), such that:

$$\tau = \boldsymbol{J}^T \boldsymbol{f} + \frac{\partial \epsilon(\boldsymbol{q}, \Delta p)}{\partial \boldsymbol{q}} \tag{4.4}$$

Note that the above equation holds when the friction force is negligible with respect to $\boldsymbol{f}$ [49]. In our application, due to the large friction at the entry port and the Columbus friction force between the tubes, compared to the interaction force of the robot with the environment, the static force mapping of Eq. (4.4) does not hold. In other words, we cannot map the tip force of the robot to the joint force or torque with the existing methods, which is fundamental for many control strategies in the robotics literature.

We will now propose and alternative approach to the compliance control of CTR via kinematic control in an implicit way. The idea of implicit and explicit force control through soft contact with the environment can be depicted in Fig. 4.2.

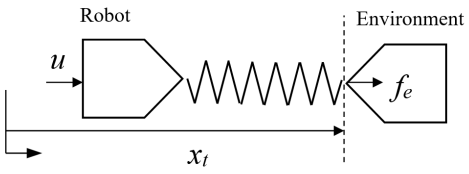

Figure 4.2: The implicit $u = q(t)$ and explicit $u = f(t)$ interaction control with the environment

The explicit force control is referred to as the case when the end effector force is controlled directly by joint torque/force. In implicit force control, on the other hand, the desired force is controlled in task space indirectly via joint displacement as the input to the robot [97]. Note that

most of the existing control algorithms for the robots are based on the explicit approach, and there is not much work on the implicit force control approach. One of the early results on implicit force control is given in [98] for a space robot application. Having passive compliance at the tip decouples the robot dynamics from the interaction with the environment, and the problem can be described in the motion control context [99]. Additionally, the robot actuation system disturbances such as nonlinear friction are rejected by the motion controller to a great extent.

4.3 Simultaneous Force/Position Control Schemes

Due to the high sensitivity of the vitreoretinal operations, we need to accurately control both position and force. Thus, simultaneous force and position control provide more precise results than impedance and stiffness control methods. The most common types of simultaneous force/position control methods in industry and medical applications are hybrid force/position control [39], external loop force/position control [43] and parallel force/position control [44]. A common feature of simultaneous force/position control methods is that, at the equilibrium, the force can be regulated to a desired constant value at the expense of a position error. Additionally, the position controller ensures the robot follows a prescribed trajectory within the robot workspace.

4.3.1 Hybrid force/position control

Hybrid position/force control controls force and position along with the constrained and unconstrained task space directions, respectively. In other words, the directions under position control are completely decoupled from those under force control in the task space. This method requires a diagonal binary selection matrix $\boldsymbol{S}_{d\times d}$, where d is the DoF in the task space. For the DoF under force control we have $s_i = 1$ and for those under position control $s_i = 0$. As observed in Fig. 4.3, the hybrid force/position control has two decoupled control loops; one for the position and one for the force. In the force control loop, the output of the controller is mapped to the actuator force or torque using the transpose of the Jacobian $\boldsymbol{J}^T$. In the position control loop, the position error in the task space is first mapped to the joint space coordinates using the inverse of the Jacobian $\boldsymbol{J}^{-1}$, and the joint space controller generates the required joint space torque or force. The resultant control

input, the sum of the force and position control loop inputs, is then fed to the robot.

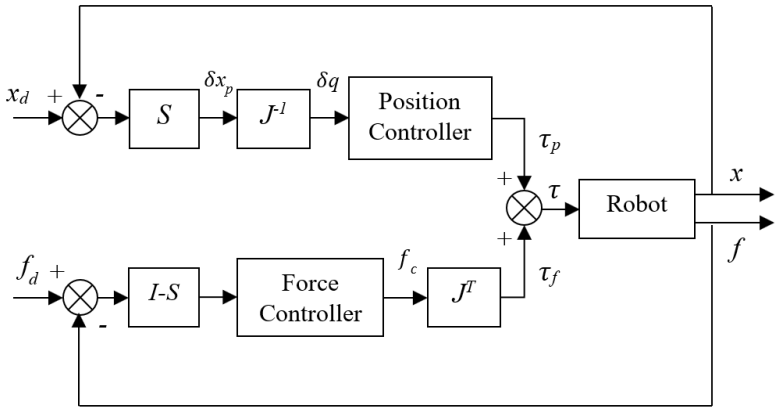

Figure 4.3: Hybrid force/position control scheme

4.3.2 Parallel force/position control

The idea of parallel force control is to design a force control action that prevails the position control action [44]. As the controller is coupled in this strategy, there might be a conflict between the two control actions. Prioritizing a control action, in that case, is performed by suitable modulation of the gains of the controllers' position and force feedback loops. The dominance of the force control over the position control loop can be achieved by having a PI controller for the force and PD controller for the position. As shown in Fig. 4.4, the original parallel force/position control method does not require a selection matrix.

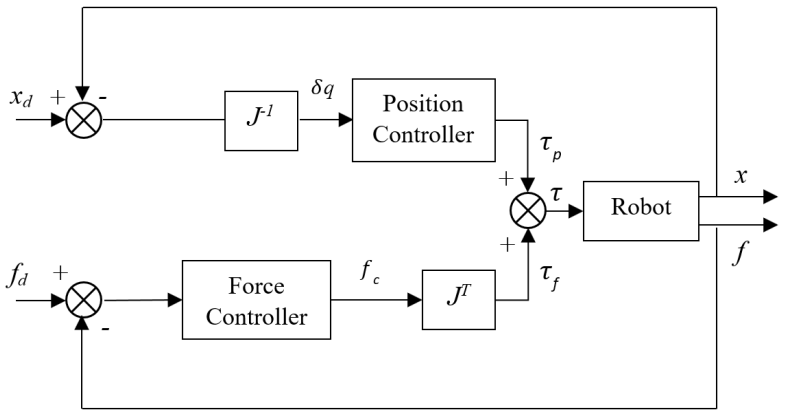

Figure 4.4: Parallel force/position control scheme

In parallel force/position, we can also have a selection matrix for the force control loop. Such a structure allows position control in all the directions in the task space; however, the force control works in certain directions specified by the selection matrix, as demonstrated in Fig. 4.5.

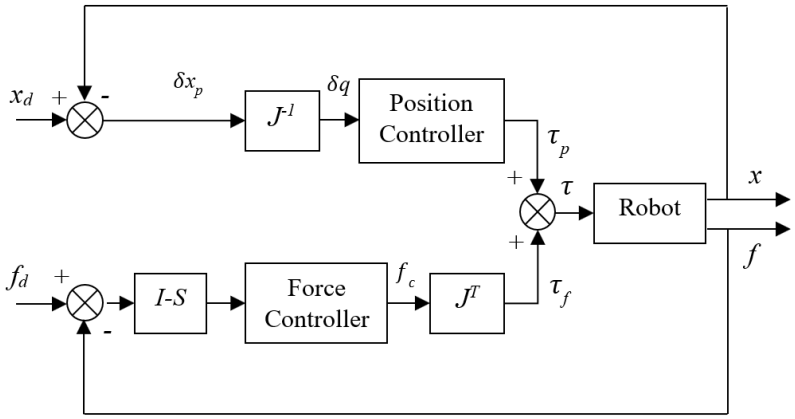

Figure 4.5: Partial hybrid force/position control scheme

4.3.3 External loop force/position control

The external position/force control allows simultaneous control of force and position in the same direction. As observed from Fig. 4.6, it consists of an inner position control loop enclosed inside an outer force controller. The output of the force controller modifies the reference value of the inner position controller. It is relatively easy to implement and requires a rather small amount of computation, and can be used in industrial robots with keeping their conventional controllers [42].

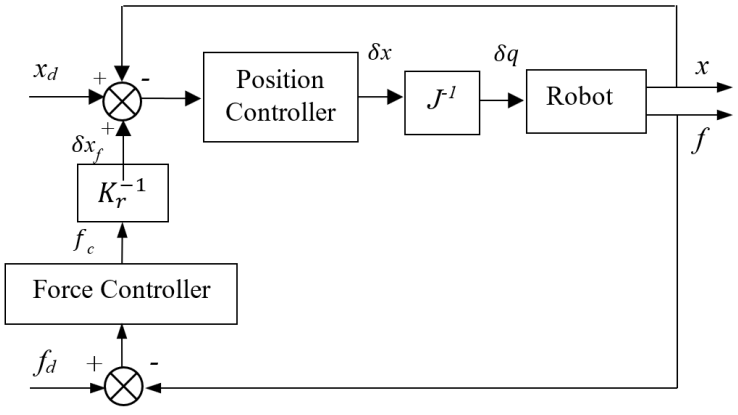

Figure 4.6: External loop force/position control

4.4 Proposed Control Architecture

As discussed earlier, the simultaneous force/position control of CRs is significantly different from the discussed control algorithm available for rigid manipulators in the previous section. In the original structure of the hybrid and parallel control, the outputs of the force control and the position control loops are force or torque. However, as discussed in Section 4.2, for CTR, which is the focus of this study, we cannot map the compensation force in task space to that of the joint space. By designing a task space controller, using the method developed in the previous chapter for the Cartesian stiffness and tip force estimation, the force controller output $\boldsymbol{\delta} f$ is mapped to Cartesian displacement through the following equation:

$$\delta \boldsymbol{x}_f = \boldsymbol{K}_r^{-1} \delta f \tag{4.5}$$

in which $\boldsymbol{K}_r$ is the resultant stiffness of the robot $\boldsymbol{K}$ and the environment $\boldsymbol{K}_e$ at the contact point defined as:

$$\boldsymbol{K}_r^{-1} = \boldsymbol{K}^{-1} + \boldsymbol{K}_e^{-1} \tag{4.6}$$

and $\boldsymbol{\delta} f$ can be obtained from a suitable control law such as PID controller as follow:

$$\boldsymbol{\delta} f = \boldsymbol{\delta} f_d + \boldsymbol{K}_p(\boldsymbol{f}_d - \boldsymbol{f}) + \boldsymbol{K}_i \int_0^t (\boldsymbol{f}_d - \boldsymbol{f}) d\xi \tag{4.7}$$

Now we design a task space controller for the position with displacement as the control output as follows:

$$\delta \boldsymbol{x}_p = \delta \boldsymbol{x}_d + \boldsymbol{K}_p'(\boldsymbol{x}_d - \boldsymbol{x}) + \boldsymbol{K}_i' \int_0^t (\boldsymbol{x}_d - \boldsymbol{x}) d\xi \tag{4.8}$$

Note that the discussed above control laws for the position and force control loops have a second order error dynamics. As an example for the position control law the error dynamics is as follows:

$$\ddot{\boldsymbol{e}} + \boldsymbol{K}_p' \dot{\boldsymbol{e}} + \boldsymbol{K}_i' \boldsymbol{e} = 0 \tag{4.9}$$

for which we can choose suitable $\boldsymbol{K}_p'$ and $\boldsymbol{K}_i'$ to have an asymptotically stable response, i.e., $\boldsymbol{K}_p', \boldsymbol{K}_i' > 0$. Using the output of the force and position control loops the overall compensation

will be:

$$\delta \boldsymbol{x}_t = \delta \boldsymbol{x}_p + \delta \boldsymbol{x}_f \tag{4.10}$$

This is the required compensation at the task space, which is then mapped to the joint space using the inverse of the Jacobian such that:

$$\delta \boldsymbol{q} = \boldsymbol{J}^{-1} \delta \boldsymbol{x}_t \tag{4.11}$$

Note that for the redundant robot, in which there are more than one configuration at the joint space to reach a specified position at the task space, $\delta \boldsymbol{q}$ is not unique. Thus, one can use the redundancy resolution methods for a suitable solution, considering the existing constraints. In the following, we apply the above methodology to control architectures discussed in Section 4.3 for indirect simultaneous force/position control of CRs.

4.4.1 Indirect simultaneous force/position control

The discussed control strategy can be applied to the hybrid control structure as shown in Fig. 4.7. This architecture devises two independent control loops in robot task space, for position and force, decoupled via selection matrix $\boldsymbol{S}$. The position control loop devises the control law of Eq. (4.8) with displacement as the output. Additionally, the force control loop controller is that of Eq. (4.7), which is converted to displacement compensation using Eq. (4.5). The summation of the task space compensation from Eq. (4.10) $\delta \boldsymbol{x}$ is then mapped to the joint space using $\boldsymbol{J}^{-1}$ to obtain joint displacements $\delta \boldsymbol{q}$ to be given to the robot. Additionally, the interaction force $\boldsymbol{f}$ is estimated indirectly using the Cartesian stiffness of the robot $\boldsymbol{K}$ and the deflection of the tip point $\Delta \boldsymbol{p}$. The deflection of the robot tip point can be found by knowing the tip end of the robot through Eq. (4.3) and its no-load tip end position $g(x, y)_{s=S}$.

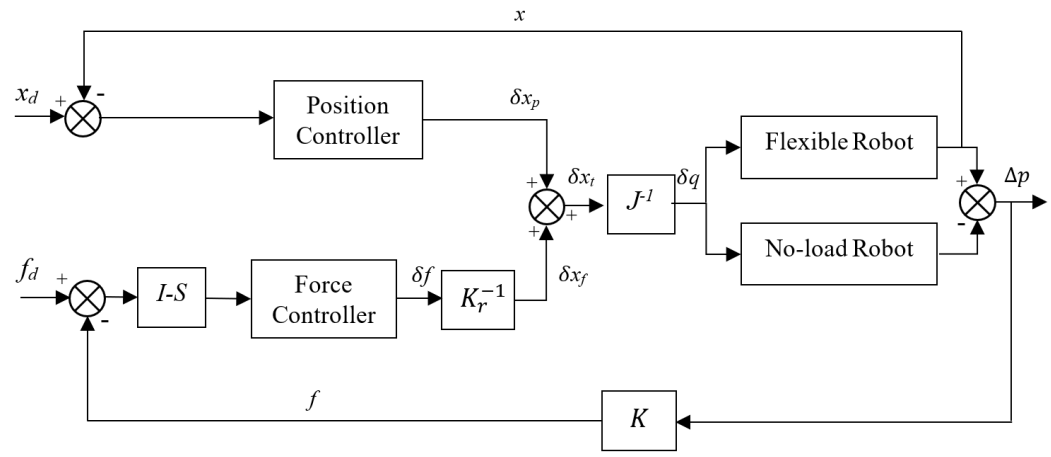

Figure 4.8: Partial hybrid force/position control strategy for CRs with position input to the robot

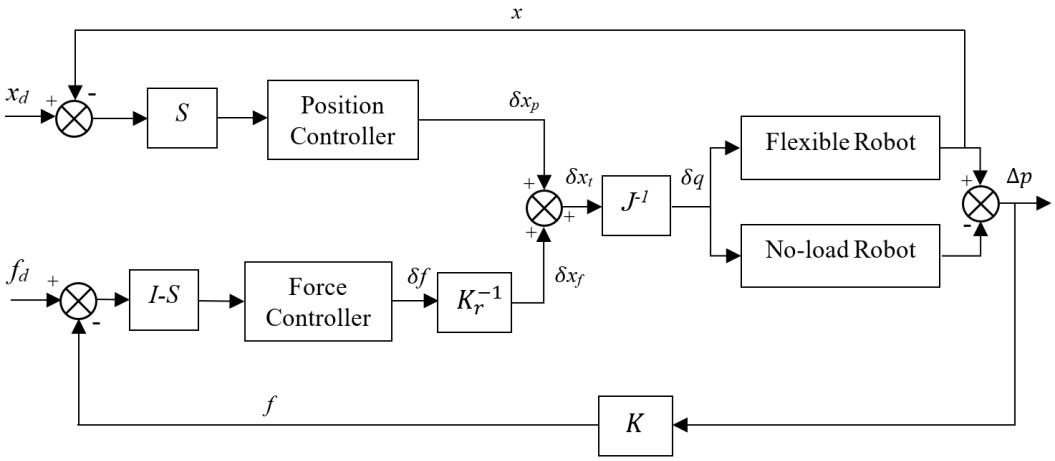

Figure 4.7: Hybrid force/position control strategy for CRs with position input to the robot

Another topology based on the hybrid force/position control is partial hybrid force/position control, as shown in Fig. 4.8. In this framework, the direction of the force control is prespecified, while we have position control in all the directions in the task space. In such a structure, as the force control should be dominant over the position control, the control gains should be selected accordingly.

The structure of the parallel force/position controller is demonstrated in Fig. 4.9. Note that the selection matrices are removed from both the position and force control loop, and the position and force controllers operate in parallel. As there might be control conflict in the position and force, the appropriate selection of the controller gain is of great importance. The performance of such a

controller can be improved using an adaptive strategy to tune the gain of the controller and keep the dominance of the force control loop.

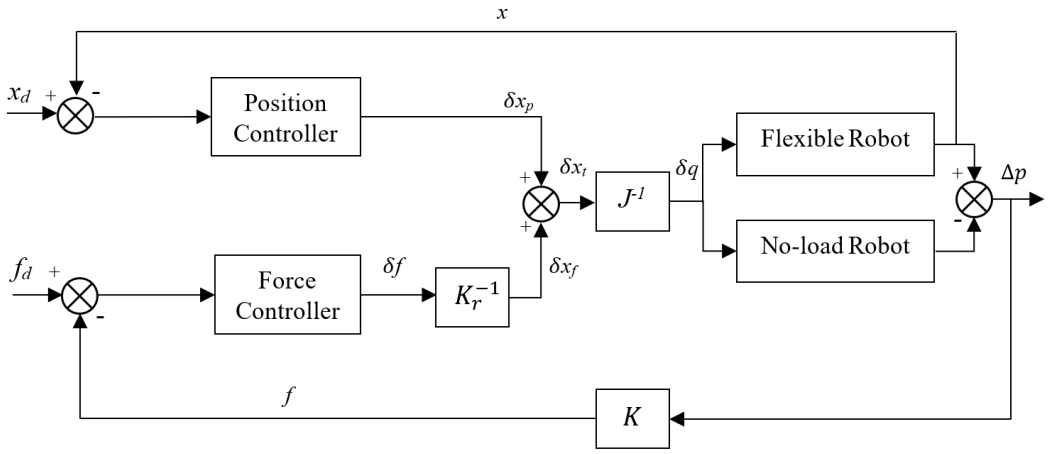

Figure 4.9: Parallel force/position control strategy for CRs with position input to the robot

The external loop controller follows the same strategy as the hybrid and parallel control, and we can consider the force controller with or without the selection matrix. As discussed for the parallel controller, the gains of the position and force loops should be selected properly so that the force control loop prevails.

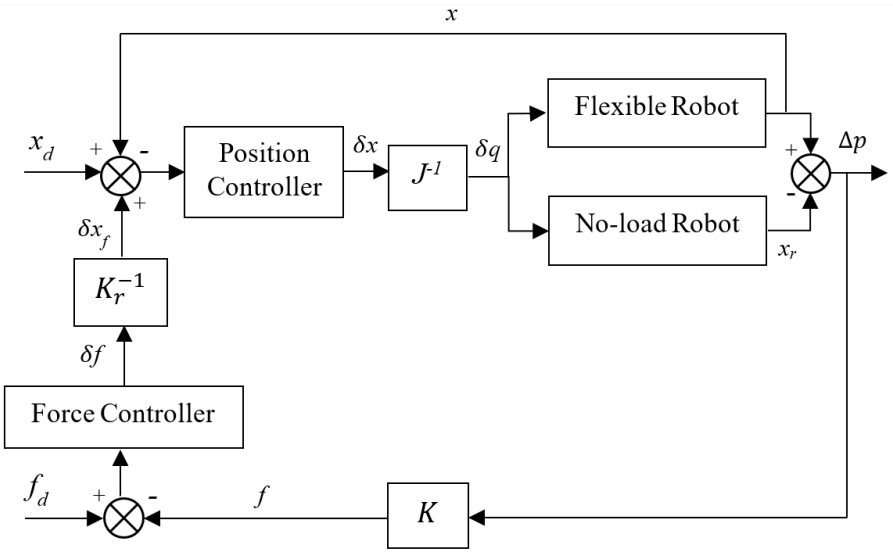

Figure 4.10: External loop force/position control strategy for CRs with position input to the robot

As discussed earlier, due to the high sensitivity of the eye surgery procedure, we need to have

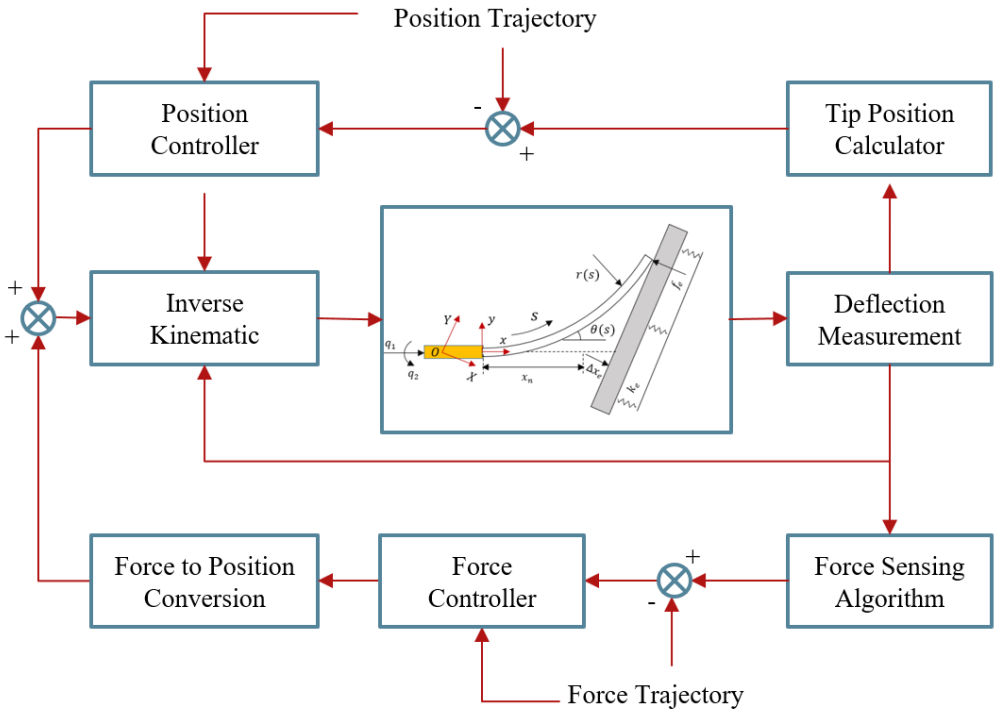

Figure 4.11: Simulation setup of the proposed closed loop indirect hybrid force/position control

precise control over force and position. Thus, hybrid force/position control can be considered a suitable candidate. Using the modified position-based hybrid force controller developed in this section (see Fig. 4.7), the proposed control architecture for the hybrid eye surgery robot discussed in Section 4.1.1 will be as Fig. 4.11.

In the proposed architecture, we emulate the real setup for the surgery. As depicted in Fig. 4.1, we have a robot with a rigid hollow shaft from which an initially-curved flexible element can be guided. The parameters of the flexible segment are similar to the inner tube described in Section 2.4.2 with the same pseudo-rigid body (PRB) parameters as in Section 2.4.5 for a variable-length highly flexible members (HFM). Additionally, the control input is applied to the continuum model developed in the first section of this chapter (Eq. (4.3)). Furthermore, the only feedback signal is the tip position of the robot, which is obtained by solving the continuum model. In practice, the tip point can be found using an electromagnetic or optical tracking system [100]. The inputs to the robot are provided using high-gain servo motors, which are high-precision position-controlled

actuators. This means that the inputs to the robot are of displacement type, contrary to the conventional control schemes with the force or torque inputs. It is desired to design a control law so that the robot tip follows a trajectory tangent to a flexible surface and applies a desired force normal to the surface. The control architecture comprises two control loops that are decoupled in task space. The obtained control input in the task space should be mapped to the actuator's effort, which in our case should be of displacement form. To this aim, we need to have the resultant stiffness of the robot tip with the environment, which can be obtained using Eq. (4.6). Knowing the resultant stiffness, the required compensation force $\delta \boldsymbol{f}$, which is the output of the force controller due to force error e_f, is mapped to the displacement $\delta \boldsymbol{x}_f$. Similarly, the position control loop generates the required displacement in the task space $\delta \boldsymbol{x}_p$ to compensate for the position error e_p. As the actuators at the joint should compensate for e_f and e_p, the compensation in the task space $\delta \boldsymbol{x}_t = \delta \boldsymbol{x}_f + \delta \boldsymbol{x}_p$ is to be mapped to the joint space, for which we use the inverse of the Jacobian in the deformed configuration. Using the Jacobian mapping, we obtain q_is as the control inputs to the system. Note that in our proposed control methodology, we use a simplified model $f_e = \boldsymbol{K}_r \Delta p$ for the control design, which is, in fact, governed by a BVP in Eq. (4.3). Thus, the controller is exposed to unmodeled dynamics. On the other hand, with a position-controlled actuator, we compensate for the friction at the entry point and among the concentric tubes.

4.5 Simulation study

To investigate the force/position tracking performance of the proposed control strategy, we consider two case studies in two different working modes of the robot described in Section 4.1.1 as follows:

First Case: In this case, the length of the flexible element of the robot is fixed, and the control inputs to the robot are q_1 and q_2. In other words, the robot is controlled via the insertion and rotation of the rigid segment.

Second Case: In the second case, the length of the flexible element of the robot is variable, and the control inputs to the robot are q_2 and q_3. In other words, the control inputs are the rotation of the rigid segment and the insertion of the flexible element.

Note that a suitable controller should provide satisfactory tracking performance when interacting with different environments. To this end, for each of the above cases, we have evaluated force/position tracking of the proposed control strategy with different stiffness for the environment.

4.5.1 Force/position tracking performance for the first case

In this section, we use simulations to investigate the force/position tracking properties of the proposed control architecture in the first case study while the robot interacts with a very soft environment with a stiffness $k_e = 5$ N/m. The simulation is carried out for two different force/position trajectories for the soft environment. In the third study, we consider the interaction of the robot with a hard environment with stiffness $k_e = 5 \times 10^6$ N/m. The simulation study is performed for a constant curvature HFM using a 30-DoF PRB equivalent model with the parameters given in Section 2.4.5.

In the first study, we consider an exponential trajectory for the force and a cosine trajectory for the tip position. The desired and actual trajectory tracking and the tracking errors for both position and force are depicted in Fig. 4.12. As observed from Fig. 4.12, the maximum tracking error is 5 μN for the force and 2 μm for the position, which is suitable for the membrane peeling procedure.

In the second study, we consider a cosine trajectory for the force and an exponential trajectory for the tip position. The desired and actual trajectories, as well as the tracking errors for both position and force, are depicted in Fig. 4.13, demonstrating the satisfactory performance of the controller, with the maximum tracking errors of 12 μN and 0.2 μm for force and position, respectively,

In the final study for the first case, we consider an exponential trajectory for the force and a cosine trajectory for the tip position, where the robot interacts with a hard environment. The desired and actual trajectories, as well as the tracking errors for both position and force, are depicted in Fig. 4.14, showing the micron-scale tracking performance.

4.5.2 Force/position tracking performance for the second case

For the second case, we first investigate the force/position tracking performance of the proposed control architecture while the robot is interacting with a very soft environment with stiffness $k_e =$

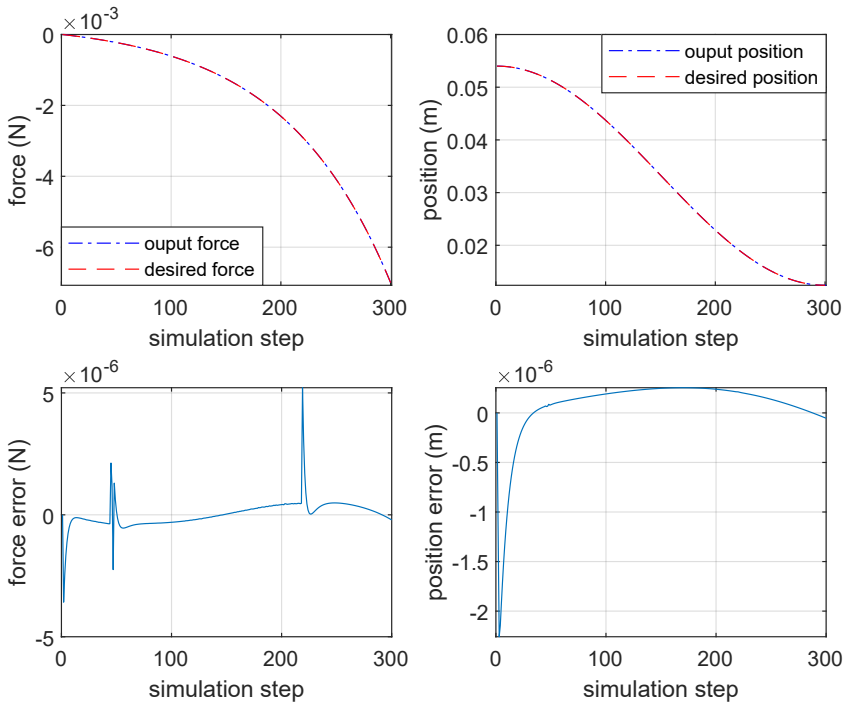

Figure 4.12: Tracking performance of the first simulation study of the first case with a soft environment

5 N/m. We then consider a harder environment with stiffness $k_e = 500$ N/m while keeping the same desired trajectories. The simulation study is performed for a variable-length constant curvature HFM using a 30-DoF PRB equivalent model with the parameters given in Section 2.4.5 where the joints stiffness is defined as a function of length. The control parameters are kept similar to the previous study. The simulation results are provided in Figs. 4.15 and 4.16, which show satisfactory tracking performance in both cases.

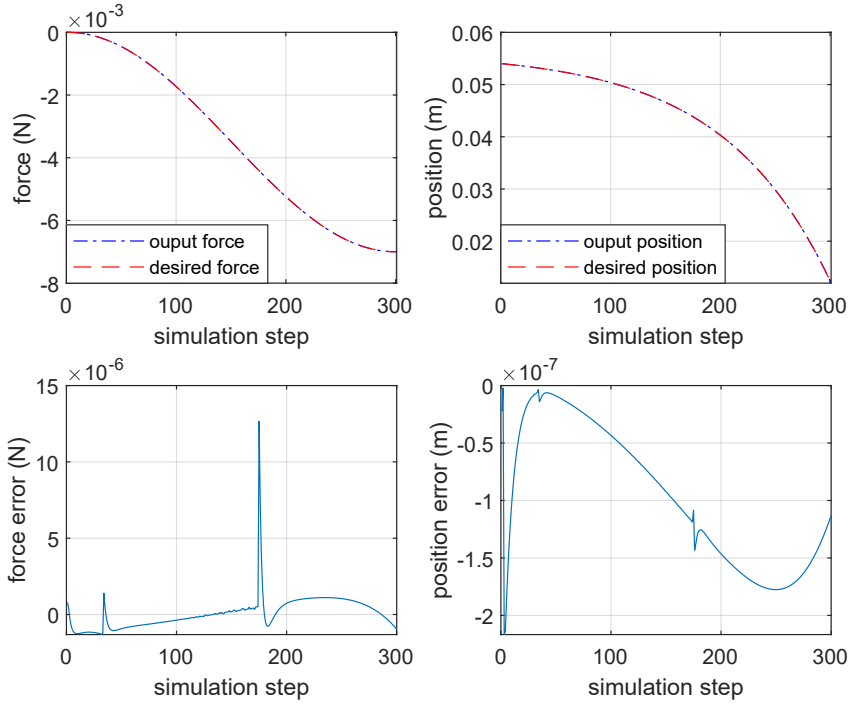

Figure 4.13: Tracking performance of the second simulation study of the first case with a soft environment

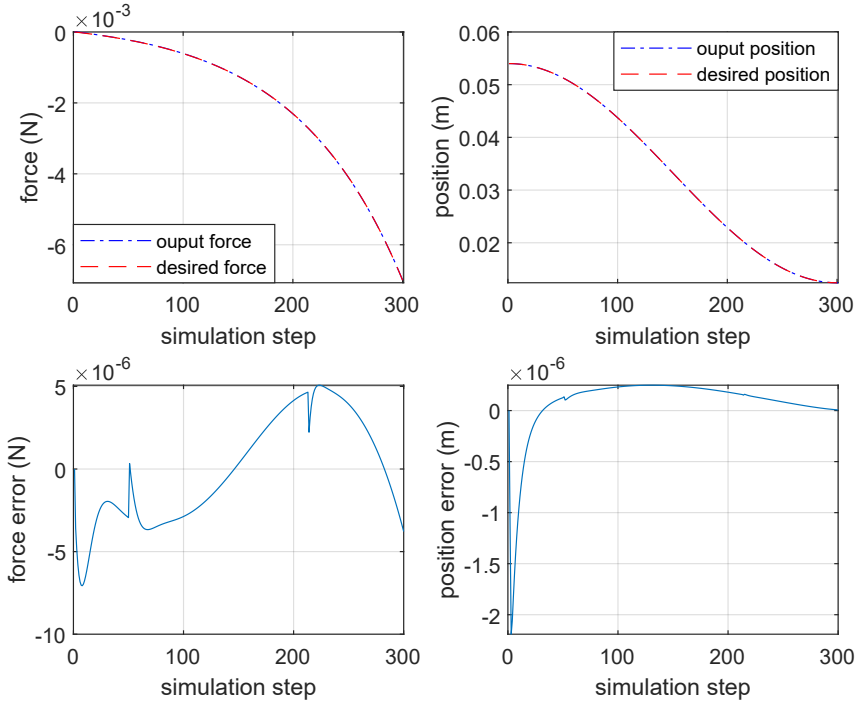

Figure 4.14: Tracking performance of the third simulation study of the first case with a hard environment

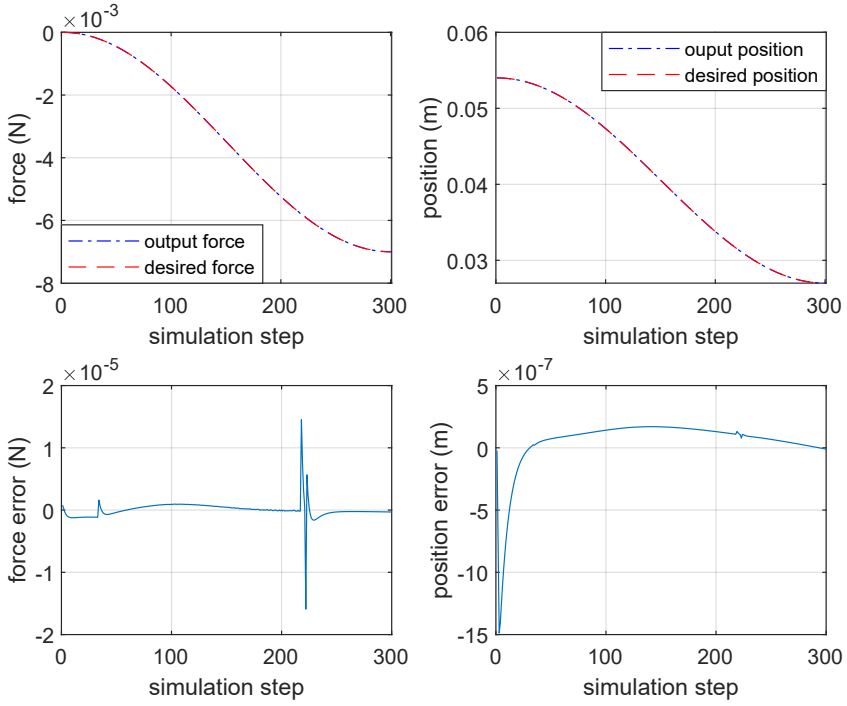

Figure 4.15: Tracking performance for the simulation study of the second case with a soft environment

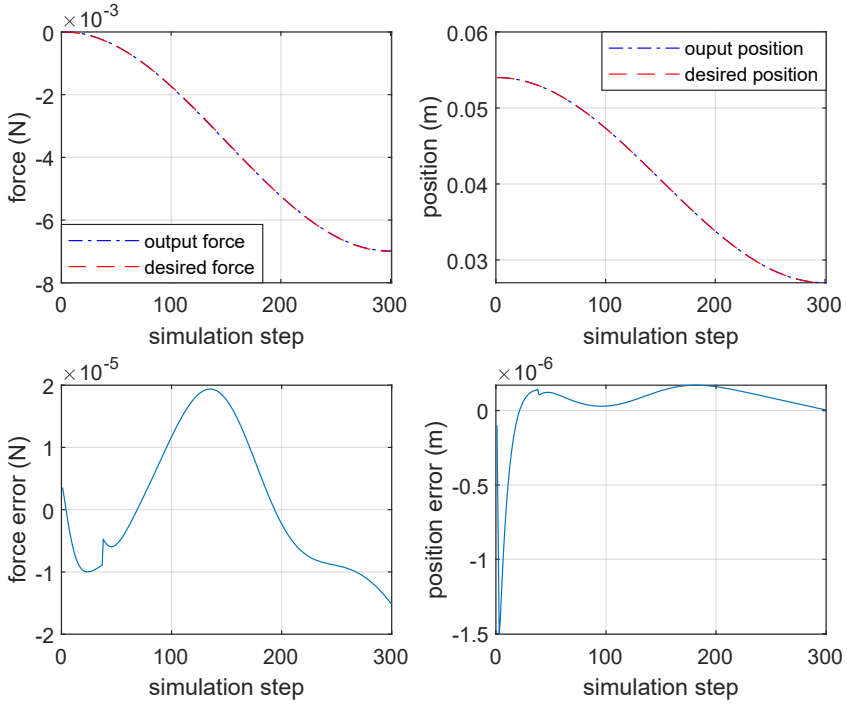

Figure 4.16: Tracking performance for the simulation study of the second case with a hard environment

Chapter 5

Conclusions and Future Works

In this doctoral thesis, we proposed an innovative approach for the simultaneous force/position control of the initially-curved, variable-length continuum robots (CR) with intrinsic force-sensing capability. The proposed approach was built upon three significant accomplishments: a) a novel semi-analytical method for pseudo-rigid-body (PRB) modeling of initially-curved variable-length CRs with variable stiffness along the length, b) a novel analytical expression for the Cartesian stiffness of the CR under large deflection, c) a new control architecture for indirect hybrid force/position control of CRs in interaction with a soft environment, using high gain position-controlled actuators. The versatility of the proposed PRB modeling approach has been proved by applying it in five different case studies, namely straight highly flexible member (HFM), circular HFM, straight HFM with variable stiffness, initially-curved HFM, and variable-length fixed curvature HFM. We also showed that the proposed formulation for the Cartesian stiffness could estimate the tip force just by knowing the tip deflection with much higher accuracy than other stiffness formulations. The performance of the proposed indirect hybrid force/position is also evaluated on a continuum model, which considers the interaction of the robot with a soft environment. The proposed control scheme was evaluated in two different cases and applied in two environments, highly soft and stiff. We had suitable tracking performance for all the scenarios for both the force and the position.

5.1 Future works

This research work can be potentially extended by:

- Experimentally evaluating the proposed PRB model and offering a reasonable number of experiments for a reliable result.
- Extending the proposed PRB modeling approach for the 3D HFMs, by including out of plane deformation of the HFMs.
- Empirical evaluation of the controller performance.
- Designing advanced controller to estimate the compliance of the environment.

Bibliography

[1] D. B. Camarillo, T. M. Krummel, and J. K. Salisbury, "Robotic technology in surgery: past, present, and future," *The American Journal of Surgery*, vol. 188, no. 4, pp. 2–15, 2004.

[2] K. Fuchs, "Minimally invasive surgery," *Endoscopy*, vol. 34, no. 2, pp. 154–159, 2002.

[3] J. Dankelman, C. A. Grimbergen, and H. G. Stassen, *Engineering for patient safety: Issues in minimally invasive procedures*. CRC Press, 2004.

[4] A. R. Lanfranco, A. E. Castellanos, J. P. Desai, and W. C. Meyers, "Robotic surgery: a current perspective," *Annals of surgery*, vol. 239, no. 1, p. 14, 2004.

[5] C. J. Payne and G.-Z. Yang, "Hand-held medical robots," *Annals of biomedical engineering*, vol. 42, no. 8, pp. 1594–1605, 2014.

[6] J. A. Smith, J. Jivraj, R. Wong, and V. Yang, "30 years of neurosurgical robots: Review and trends for manipulators and associated navigational systems," *Annals of biomedical engineering*, vol. 44, no. 4, pp. 836–846, 2016.

[7] H. Rafii-Tari, C. J. Payne, and G.-Z. Yang, "Current and emerging robot-assisted endovascular catheterization technologies: a review," *Annals of biomedical engineering*, vol. 42, no. 4, pp. 697–715, 2014.

[8] R. H. Taylor, J. Funda, L. Joskowicz, A. D. Kalvin, S. H. Gomory, A. Gueziec, and L. M. Brown, "An overview of computer-integrated surgery at the ibm thomas j. watson research center," *IBM journal of research and development*, vol. 40, no. 2, pp. 163–183, 1996.

[9] A. Molaei, E. Abedloo, H. D. Taghirad, and Z. Marvi, "Kinematic and workspace analysis of diamond: An innovative eye surgery robot," in *2015 23rd Iranian conference on electrical engineering*. IEEE, 2015, pp. 882–887.

[10] P. E. Dupont, J. Lock, B. Itkowitz, and E. Butler, "Design and control of concentric-tube robots," *IEEE Transactions on Robotics*, vol. 26, no. 2, pp. 209–225, 2010.

[11] P. Dupont, N. Simaan, H. Choset, and C. Rucker, "Continuum robots for medical interventions," *Proceedings of the IEEE*, 2022.

[12] J. Burgner-Kahrs, D. C. Rucker, and H. Choset, "Continuum robots for medical applications: A survey," *IEEE Transactions on Robotics*, vol. 31, no. 6, pp. 1261–1280, 2015.

[13] Z. Mitros, S. H. Sadati, R. Henry, L. Da Cruz, and C. Bergeles, "From theoretical work to clinical translation: Progress in concentric tube robots," *Annual Review of Control, Robotics, and Autonomous Systems*, vol. 5, 2021.

[14] A. Garriga-Casanovas and F. Rodriguez y Baena, "Complete follow-the-leader kinematics using concentric tube robots," *The International Journal of Robotics Research*, 2017.

[15] H. B. Gilbert, R. J. Hendrick, and R. J. Webster III, "Elastic stability of concentric tube robots: A stability measure and design test," *IEEE Transactions on Robotics*, vol. 32, no. 1, pp. 20–35, 2016.

[16] J. Burgner, P. J. Swaney, R. A. Lathrop, K. D. Weaver, and R. J. Webster, "Debulking from within: a robotic steerable cannula for intracerebral hemorrhage evacuation," *IEEE Transactions on Biomedical Engineering*, vol. 60, no. 9, pp. 2567–2575, 2013.

[17] J. Burgner, D. C. Rucker, H. B. Gilbert, P. J. Swaney, P. T. Russell, K. D. Weaver, and R. J. Webster, "A telerobotic system for transnasal surgery," *IEEE/ASME Transactions on Mechatronics*, vol. 19, no. 3, pp. 996–1006, 2014.

[18] A. H. Gosline, N. V. Vasilyev, E. J. Butler, C. Folk, A. Cohen, R. Chen, N. Lang, P. J. Del Nido, and P. E. Dupont, "Percutaneous intracardiac beating-heart surgery using metal

mems tissue approximation tools," *The International journal of robotics research*, vol. 31, no. 9, pp. 1081–1093, 2012.

[19] J. Burgner, P. J. Swaney, T. L. Bruns, M. S. Clark, D. C. Rucker, E. C. Burdette, and R. J. Webster, "An autoclavable steerable cannula manual deployment device: Design and accuracy analysis," *Journal of medical devices*, vol. 6, no. 4, p. 041007, 2012.

[20] R. J. Hendrick, S. D. Herrell, and R. J. Webster, "A multi-arm hand-held robotic system for transurethral laser prostate surgery," in *Robotics and Automation (ICRA), 2014 IEEE International Conference on*. IEEE, 2014, pp. 2850–2855.

[21] T. L. Bruns, A. A. Remirez, M. A. Emerson, R. A. Lathrop, A. W. Mahoney, H. B. Gilbert, C. L. Liu, P. T. Russell, R. F. Labadie, K. D. Weaver *et al.*, "A modular, multi-arm concentric tube robot system with application to transnasal surgery for orbital tumors," *The International Journal of Robotics Research*, vol. 40, no. 2-3, pp. 521–533, 2021.

[22] W. Wei, R. Goldman, N. Simaan, H. Fine, and S. Chang, "Design and theoretical evaluation of micro-surgical manipulators for orbital manipulation and intraocular dexterity," in *Proceedings 2007 IEEE international conference on robotics and automation*. IEEE, 2007.

[23] W. Wei, R. E. Goldman, H. F. Fine, S. Chang, and N. Simaan, "Performance evaluation for multi-arm manipulation of hollow suspended organs," *IEEE transactions on robotics*, vol. 25, no. 1, pp. 147–157, 2008.

[24] L. Wu, B. L.-W. Tan, and H. Ren, "Prototype development of a hand-held robotic light pipe for intraocular procedures," in *2015 IEEE international conference on robotics and biomimetics (ROBIO)*. IEEE, 2015, pp. 368–373.

[25] F.-Y. Lin, C. Bergeles, and G.-Z. Yang, "Biometry-based concentric tubes robot for vitreoretinal surgery," in *Engineering in Medicine and Biology Society (EMBC), 2015 37th Annual International Conference of the IEEE*. IEEE, 2015, pp. 5280–5284.

[26] C. Bergeles, M. Sugathapala, and G.-Z. Yang, "Retinal surgery with flexible robots: Biomechanical advantages," in *2018 International Symposium on Medical Robotics (ISMR)*. IEEE, 2018, pp. 1–6.

[27] K. Xu and N. Simaan, "An investigation of the intrinsic force sensing capabilities of continuum robots," *IEEE Transactions on Robotics*, vol. 24, no. 3, pp. 576–587, 2008.

[28] ——, "Intrinsic wrench estimation and its performance index for multisegment continuum robots," *IEEE Transactions on Robotics*, vol. 26, no. 3, pp. 555–561, 2010.

[29] A. Bajo and N. Simaan, "Hybrid motion/force control of multi-backbone continuum robots," *The International journal of robotics research*, vol. 35, no. 4, pp. 422–434, 2016.

[30] A. M. Okamura, "Haptic feedback in robot-assisted minimally invasive surgery," *Current opinion in urology*, vol. 19, no. 1, p. 102, 2009.

[31] W. Wei and N. Simaan, "Modeling, force sensing, and control of flexible cannulas for microstent delivery," *Journal of Dynamic Systems, Measurement, and Control*, vol. 134, no. 4, p. 041004, 2012.

[32] D. C. Rucker and R. J. Webster, "Deflection-based force sensing for continuum robots: A probabilistic approach," in *2011 IEEE/RSJ International Conference on Intelligent Robots and Systems*. IEEE, 2011, pp. 3764–3769.

[33] S. Hasanzadeh and F. Janabi-Sharifi, "Model-based force estimation for intracardiac catheters," *IEEE/ASME Transactions on Mechatronics*, vol. 21, no. 1, pp. 154–162, 2015.

[34] P. K. Gupta, P. S. Jensen, and E. de Juan, "Surgical forces and tactile perception during retinal microsurgery," in *International Conference on Medical Image Computing and Computer-Assisted Intervention*. Springer, 1999, pp. 1218–1225.

[35] X. He, I. Iordachita, R. H. Taylor, J. T. Handa, and P. L. Gehlbach, "Tool and tool system having independent axial and transverse force sensing," Jul. 30 2019, uS Patent 10,363,164.

[36] M. Balicki, A. Uneri, I. Iordachita, J. Handa, P. Gehlbach, and R. Taylor, "Micro-force sensing in robot assisted membrane peeling for vitreoretinal surgery," in *International Conference on Medical Image Computing and Computer-Assisted Intervention*. Springer, 2010, pp. 303–310.

[37] M. Schumacher, J. Wojtusch, P. Beckerle, and O. von Stryk, "An introductory review of active compliant control," *Robotics and Autonomous Systems*, vol. 119, pp. 185–200, 2019.

[38] J. K. Salisbury, "Active stiffness control of a manipulator in cartesian coordinates," in *1980 19th IEEE conference on decision and control including the symposium on adaptive processes*. IEEE, 1980, pp. 95–100.

[39] M. H. Raibert and J. J. Craig, "Hybrid position/force control of manipulators," *ASME Transactions on Dynamic Systems, Measurement, Control*, 1981.

[40] M. T. Mason, "Compliance and force control for computer controlled manipulators," *IEEE Transactions on Systems, Man, and Cybernetics*, vol. 11, no. 6, pp. 418–432, 1981.

[41] T. Yoshikawa, "Force control of robot manipulators," in *Proceedings 2000 ICRA. Millennium Conference. IEEE International Conference on Robotics and Automation. Symposia Proceedings (Cat. No. 00CH37065)*, vol. 1. IEEE, 2000, pp. 220–226.

[42] W. Khalil and E. Dombre, *Modeling, identification and control of robots*. Butterworth-Heinemann, 2004.

[43] J. De Schutter and H. Van Brussel, "Compliant robot motion ii. a control approach based on external control loops," *The International Journal of Robotics Research*, vol. 7, no. 4, pp. 18–33, 1988.

[44] S. Chiaverini and L. Sciavicco, "The parallel approach to force/position control of robotic manipulators," *IEEE Transactions on Robotics and Automation*, vol. 9, no. 4, pp. 361–373, 1993.

[45] G. Smoljkic, G. Borghesan, D. Reynaerts, J. De Schutter, J. Vander Sloten, and E. Vander Poorten, "Constraint-based interaction control of robots featuring large compliance and deformation," *IEEE Transactions on Robotics*, vol. 31, no. 5, pp. 1252–1260, 2015.

[46] M. Mahvash and P. E. Dupont, "Stiffness control of surgical continuum manipulators," *IEEE Transactions on Robotics*, vol. 27, no. 2, pp. 334–345, 2011.

[47] S. B. Kesner and R. D. Howe, "Force control of flexible catheter robots for beating heart surgery," in *2011 IEEE international conference on robotics and automation*. IEEE, 2011, pp. 1589–1594.

[48] M. C. Yip, J. A. Sganga, and D. B. Camarillo, "Autonomous control of continuum robot manipulators for complex cardiac ablation tasks," *Journal of Medical Robotics Research*, vol. 2, no. 01, p. 1750002, 2017.

[49] A. W. Mahoney, H. B. Gilbert, and R. J. Webster III, "A review of concentric tube robots: modeling, control, design, planning, and sensing," *The Encyclopedia of MEDICAL ROBOTICS: Volume 1 Minimally Invasive Surgical Robotics*, pp. 181–202, 2019.

[50] J. H. P. G. R. H. T. Ali Uneri, Marcin A. Balicki and I. Iordachita, "New steady-hand eye robot with micro-force sensing for vitreoretinal surgery," in *2010 IEEE international conference on Biomedical Robotics and Biomechatronics*. IEEE, 2010, pp. 1589–1594.

[51] C. Haritoglou, C. A. Gass, M. Schaumberger, A. Gandorfer, M. W. Ulbig, and A. Kampik, "Long-term follow-up after macular hole surgery with internal limiting membrane peeling," *American journal of ophthalmology*, vol. 134, no. 5, pp. 661–666, 2002.

[52] A. Pashkevich, A. Klimchik, and D. Chablat, "Enhanced stiffness modeling of manipulators with passive joints," *Mechanism and machine theory*, vol. 46, no. 5, pp. 662–679, 2011.

[53] A. Raoofian, A. Taghvaeipour, and A. Kamali, "On the stiffness analysis of robotic manipulators and calculation of stiffness indices," *Mechanism and Machine Theory*, vol. 130, pp. 382–402, 2018.

[54] A. Senthil Kumar, M. Aravind Raghavendra, W. Neo, and M. Rahman, "Fast and fine tool servo for ultraprecision machining in comprehensive materials processing," *Rahman M, editor*, vol. 11, pp. 61–88, 2014.

[55] L. L. Howell, *Compliant mechanisms*. John Wiley & Sons, 2001.

[56] M. Khoshnam and R. V. Patel, "A pseudo-rigid-body 3r model for a steerable ablation catheter," in *2013 IEEE International Conference on Robotics and Automation*. IEEE, 2013, pp. 4427–4432.

[57] T. Greigarn, R. Jackson, T. Liu, and M. C. Çavuşoğlu, "Experimental validation of the pseudo-rigid-body model of the mri-actuated catheter," in *2017 IEEE International Conference on Robotics and Automation (ICRA)*. IEEE, 2017, pp. 3600–3605.

[58] V. K. Venkiteswaran, J. Sikorski, and S. Misra, "Shape and contact force estimation of continuum manipulators using pseudo rigid body models," *Mechanism and machine theory*, vol. 139, pp. 34–45, 2019.

[59] V. K. Venkiteswaran and H.-J. Su, "Pseudo-rigid-body models for circular beams under combined tip loads," *Mechanism and Machine Theory*, vol. 106, pp. 80–93, 2016.

[60] V. K. Venkiteswaran and H. J. Su, "A versatile 3r pseudo-rigid-body model for initially curved and straight compliant beams of uniform cross section," *Journal of Mechanical Design*, vol. 140, no. 9, 2018.

[61] J. Lock and P. E. Dupont, "Friction modeling in concentric tube robots," in *2011 IEEE International Conference on Robotics and Automation*. IEEE, 2011, pp. 1139–1146.

[62] P. Wang and Q. Xu, "Design and modeling of constant-force mechanisms: A survey," *Mechanism and Machine Theory*, vol. 119, pp. 1–21, 2018.

[63] Y.-J. Park, U. Jeong, J. Lee, S.-R. Kwon, H.-Y. Kim, and K.-J. Cho, "Kinematic condition for maximizing the thrust of a robotic fish using a compliant caudal fin," *IEEE Transactions on Robotics*, vol. 28, no. 6, pp. 1216–1227, 2012.

[64] J. Ding, R. E. Goldman, K. Xu, P. K. Allen, D. L. Fowler, and N. Simaan, "Design and coordination kinematics of an insertable robotic effectors platform for single-port access surgery," *IEEE/ASME transactions on mechatronics*, vol. 18, no. 5, pp. 1612–1624, 2012.

[65] M. N. M. Zubir, B. Shirinzadeh, and Y. Tian, "A new design of piezoelectric driven compliant-based microgripper for micromanipulation," *Mechanism and Machine Theory*, vol. 44, no. 12, pp. 2248–2264, 2009.

[66] S. Kota, J. Joo, Z. Li, S. M. Rodgers, and J. Sniegowski, "Design of compliant mechanisms: applications to mems," *Analog integrated circuits and signal processing*, vol. 29, no. 1-2, pp. 7–15, 2001.

[67] V. K. Venkiteswaran and H.-J. Su, "Development of a 3-spring pseudo rigid body model of compliant joints for robotic applications," in *ASME 2014 International Design Engineering Technical Conferences and Computers and Information in Engineering Conference*. American Society of Mechanical Engineers Digital Collection, 2014.

[68] N. G. Tsagarakis, Z. Li, J. Saglia, and D. G. Caldwell, "The design of the lower body of the compliant humanoid robot "ccub"," in *2011 IEEE International Conference on Robotics and Automation*. IEEE, 2011, pp. 2035–2040.

[69] Y. She, D. Meng, H. Shi, and H.-J. Su, "Dynamic modeling of a 2d compliant link for safety evaluation in human-robot interactions," in *2015 IEEE/RSJ International Conference on Intelligent Robots and Systems (IROS)*. IEEE, 2015, pp. 3759–3764.

[70] S. Grazioso, G. Di Gironimo, and A. Lanzotti, "Mechanics–based virtual prototyping of robots with deformable bodies and flexible joints," in *International Conference on Design, Simulation, Manufacturing: The Innovation Exchange*. Springer, 2019, pp. 444–457.

[71] O. Altuzarra, D. Caballero, F. J. Campa, and C. Pinto, "Position analysis in planar parallel continuum mechanisms," *Mechanism and Machine Theory*, vol. 132, pp. 13–29, 2019.

[72] H.-H. Pham and I.-M. Chen, "Stiffness modeling of flexure parallel mechanism," *Precision Engineering*, vol. 29, no. 4, pp. 467–478, 2005.

[73] L. L. Howell, A. Midha, and T. W. Norton, "Evaluation of equivalent spring stiffness for use in a pseudo-rigid-body model of large-deflection compliant mechanisms," 1996.

[74] V. Kalpathy Venkiteswaran, "Development of a design framework for compliant mechanisms using pseudo-rigid-body models," Ph.D. dissertation, 2017.

[75] S. Sanan, J. B. Moidel, and C. G. Atkeson, "Robots with inflatable links," in *2009 IEEE/RSJ International Conference on Intelligent Robots and Systems*. IEEE, 2009, pp. 4331–4336.

[76] C. E. Doyle, J. J. Bird, T. A. Isom, C. J. Johnson, J. C. Kallman, J. A. Simpson, R. J. King, J. J. Abbott, and M. A. Minor, "Avian-inspired passive perching mechanism for robotic rotorcraft," in *2011 IEEE/RSJ International Conference on Intelligent Robots and Systems*. IEEE, 2011, pp. 4975–4980.

[77] S. Satheeshbabu and G. Krishnan, "Designing systems of fiber reinforced pneumatic actuators using a pseudo-rigid body model," in *2017 IEEE/RSJ International Conference on Intelligent Robots and Systems (IROS)*. IEEE, 2017, pp. 1201–1206.

[78] S. Huang, D. Meng, X. Wang, B. Liang, and W. Lu, "A 3d static modeling method and experimental verification of continuum robots based on pseudo-rigid body theory," in *2019 IEEE/RSJ International Conference on Intelligent Robots and Systems (IROS)*. IEEE, 2019, pp. 4672–4677.

[79] T. Greigarn and M. C. Çavuşoğlu, "Pseudo-rigid-body model and kinematic analysis of mri-actuated catheters," in *2015 IEEE International Conference on Robotics and Automation (ICRA)*. IEEE, 2015, pp. 2236–2243.

[80] T. Greigarn, N. L. Poirot, X. Xu, and M. C. Çavuşoğlu, "Jacobian-based task-space motion planning for mri-actuated continuum robots," *IEEE robotics and automation letters*, vol. 4, no. 1, pp. 145–152, 2018.

[81] E. Franco, T. Brown, A. Astolfi, and F. R. y Baena, "Adaptive energy shaping control of robotic needle insertion," *Mechanism and Machine Theory*, vol. 155, p. 104060, 2021.

[82] L. Howell and A. Midha, "A method for the design of compliant mechanisms with small-length flexural pivots," *Journal of Mechanical Design*, 1994.

[83] L. L. Howell and A. Midha, "Parametric deflection approximations for end-loaded, large-deflection beams in compliant mechanisms," *Journal of Mechanical Design*, 1995.

[84] H.-J. Su, "A pseudorigid-body 3r model for determining large deflection of cantilever beams subject to tip loads," *Journal of Mechanisms and Robotics*, vol. 1, no. 2, 2009.

[85] G. Chen, B. Xiong, and X. Huang, "Finding the optimal characteristic parameters for 3r pseudo-rigid-body model using an improved particle swarm optimizer," *Precision Engineering*, vol. 35, no. 3, pp. 505–511, 2011.

[86] R. Yasin and N. Simaan, "Joint-level force sensing for indirect hybrid force/position control of continuum robots with friction," *The International Journal of Robotics Research*, vol. 40, no. 4-5, pp. 764–781, 2021.

[87] M. C. Yip and D. B. Camarillo, "Model-less hybrid position/force control: a minimalist approach for continuum manipulators in unknown, constrained environments," *IEEE Robotics and Automation Letters*, vol. 1, no. 2, pp. 844–851, 2016.

[88] M. Razban, J. Dargahi, and B. Boulet, "A sensor-less catheter contact force estimation approach in endovascular intervention procedures," in *2018 IEEE/RSJ International Conference on Intelligent Robots and Systems (IROS)*, pp. 2100–2106.

[89] M. Razban and J. Dargahi, "Image-based intraluminal contact force monitoring in robotic vascular navigation," *arXiv preprint arXiv:2012.10762*, 2020.

[90] S.-F. Chen and I. Kao, "Conservative congruence transformation for joint and cartesian stiffness matrices of robotic hands and fingers," *The International Journal of Robotics Research*, vol. 19, no. 9, pp. 835–847, 2000.

[91] M. C. Yip and D. B. Camarillo, "Model-less feedback control of continuum manipulators in constrained environments," *IEEE Transactions on Robotics*, vol. 30, no. 4, pp. 880–889, 2014.

[92] ——, "Model-less hybrid position/force control: A minimalist approach for continuum manipulators in unknown, constrained environments," *IEEE Robotics and Automation Letters*, vol. 1, no. 2, pp. 844–851, 2016.

[93] H. D. Taghirad, *Parallel robots: mechanics and control*. CRC press, 2013.

[94] T.-T. Lu and S.-H. Shiou, "Inverses of 2×2 block matrices," *Computers & Mathematics with Applications*, vol. 43, no. 1-2, pp. 119–129, 2002.

[95] N. Simaan, A. Bajo, J. L. Netterville, C. G. Garrett, and R. E. Goldman, "Systems and methods for safe compliant insertion and hybrid force/motion telemanipulation of continuum robots," Jan. 10 2017, uS Patent 9,539,726.

[96] N. Simaan, R. H. Taylor, and J. T. Handa, "System and method for macro-micro distal dexterity enhancement in micro-surgery of the eye," Sep. 10 2019, uS Patent 10,406,026.

[97] J. Roy and L. L. Whitcomb, "Adaptive force control of position/velocity controlled robots: theory and experiment," *IEEE Transactions on Robotics and Automation*, vol. 18, no. 2, pp. 121–137, 2002.

[98] G. Hirzinger, B. Brunner, J. Dietrich, and J. Heindl, "Sensor-based space robotics-rotex and its telerobotic features," *IEEE Transactions on robotics and automation*, vol. 9, no. 5, pp. 649–663, 1993.

[99] J. De Schutter, D. Torfs, H. Bruyninckx, and S. Dutré, "Invariant hybrid force/position control of a velocity controlled robot with compliant end effector using modal decoupling," *The International Journal of Robotics Research*, vol. 16, no. 3, pp. 340–356, 1997.

[100] M. A. Nasseri, E. Dean, S. Nair, M. Eder, A. Knoll, M. Maier, and C. P. Lohmann, "Clinical motion tracking and motion analysis during ophthalmic surgery using electromagnetic tracking system," in *2012 5th International Conference on BioMedical Engineering and Informatics*. IEEE, 2012, pp. 1058–1062.